

Pressure-anisotropy-driven microturbulence and magnetic-field evolution in shearing, collisionless plasma

Scott Melville,^{1,2,3,4*} Alexander A. Schekochihin^{1,5†} and Matthew W. Kunz^{6,7‡}

¹*The Rudolf Peierls Centre for Theoretical Physics, University of Oxford, Oxford OX1 3NP, UK*

²*The Queen's College, Oxford OX1 4AW, UK*

³*Wolfgang Pauli Institute, University of Vienna, 1090 Vienna, Austria*

⁴*Harvard University, Cambridge, Massachusetts 02138, USA*

⁵*Merton College, Oxford OX1 4JD, UK*

⁶*Department of Astrophysical Sciences, Princeton University, Princeton, New Jersey 08544, USA*

⁷*Princeton Plasma Physics Laboratory, Princeton, New Jersey 08543, USA*

22 December 2021

ABSTRACT

The nonlinear state of a high-beta collisionless plasma is investigated in which an externally imposed linear shear amplifies or diminishes a uniform mean magnetic field, driving pressure anisotropies and, therefore, firehose or mirror instabilities. The evolution of the resulting microscale turbulence is considered when the external shear *changes*, mimicking the local behaviour of a macroscopic turbulent plasma flow, *viz.*, the shear is either switched off or reversed after one shear time, so that a new macroscale configuration is superimposed on the microscale state left behind by the previous one. It is shown that there is a threshold value of plasma beta: when $\beta \ll \Omega/S$ (ion cyclotron frequency/shear rate), the emergence of firehose or mirror fluctuations when they are driven unstable by shear and their disappearance when the shear is removed or reversed are quasi-instantaneous compared to the macroscopic (shear) timescale. This is because the free-decay time scale of these fluctuations is $\sim \beta/\Omega \ll S^{-1}$, a result that arises from the free decay of both types of fluctuations turning out to be constrained by the same marginal-stability thresholds as their growth and saturation in the driven regime. In contrast, when $\beta \gtrsim \Omega/S$ (“ultra-high” beta), the old microscale state can only be removed on the macroscopic (shear) timescale. Furthermore, it is found that in this ultra-high-beta regime, when the firehose fluctuations are driven, they grow secularly to order-unity amplitudes (relative to the mean field), this growth compensating for the decay of the mean field, with pressure anisotropy pinned at marginal stability purely by the increase in the fluctuation energy, with no appreciable scattering of particles (which is unlike what happens at moderate β). When the shear reverses, the shearing away of this firehose turbulence compensates for the increase in the mean field and thus prevents growth of the pressure anisotropy, stopping the system from going mirror-unstable. Therefore, at ultra-high β , the system stays close to the firehose threshold, the mirror instability is almost completely suppressed, while the mean magnitude of the magnetic field barely changes at all. Implications of the properties of both ultra-high- and moderate-beta regimes for the operation of plasma dynamo and thus the origin of cosmic magnetism are discussed, suggesting that collisionless effects are broadly beneficial to fast magnetic-field generation.

Key words: dynamo—magnetic fields—plasmas—turbulence—galaxies: clusters: intracluster medium

1 INTRODUCTION

In recent years, it has become increasingly clear that the dynamics of a high-beta, collisionless (or weakly collisional)

* E-mail: scott.melville@oxon.org

† E-mail: alex.schekochihin@physics.ox.ac.uk

‡ E-mail: mkunz@princeton.edu

plasma are both a poorly understood and very interesting subject. Astrophysically, this type of plasma represents most of the luminous matter in the Universe as it fills the intra-cluster medium (ICM) of the clusters of galaxies. The ICM is “high-beta” in the sense that the ratio of thermal to magnetic energy densities is large:

$$\beta = \frac{8\pi p}{B^2} \gg 1, \quad (1)$$

where p is pressure and B is magnetic-field strength (in galaxy-cluster cores, the typical values are $B \sim 10^{-6}$ G and $\beta \sim 10^2$; see, e.g., Enßlin & Vogt 2006 or Rosin et al. 2011 for a good set of fiducial ICM parameters). The reason for the large value of β is that the magnetic-energy density tends to be comparable to the energy density of the turbulent plasma motions and the latter are typically subsonic, so $\beta \sim 1/\text{Ma}^2$, where $\text{Ma} \sim 0.1$ is the Mach number (e.g., Fujita 2005; Rebusco et al. 2006; Sanders & Fabian 2013; Zhuravleva et al. 2014). The ICM is “weakly collisional” in the sense that collisions are much less frequent than the Larmor gyration,

$$\frac{\nu_{ii}}{\Omega} \ll 1, \quad (2)$$

where ν_{ii} is the ion-ion collision frequency (ICM is a hydrogen plasma) and Ω is the ion Larmor frequency (assuming ion number density $n_i \sim 10^2 \text{ cm}^{-3}$ and temperature $T \sim 10^7$ K, the ratio of these frequencies is small provided $\beta \ll 10^{24}$, or $B \gg 10^{-17}$ G).

The reason the dynamics of such plasmas are unlike those of an MHD fluid is that weak collisionality permits approximate conservation of particle adiabatic invariants and so when frozen-in magnetic field is locally increased or decreased by the plasma motions, perpendicular (p_\perp) and parallel (p_\parallel) pressures evolve differently (Chew et al. 1956; Kulsrud 1983), giving rise to local pressure anisotropies. Pressure-anisotropic plasma is unstable when the relative pressure anisotropy is large enough compared to $1/\beta$ (otherwise Lorentz forces stabilise the plasma), namely,

$$\Delta \equiv \frac{p_\perp - p_\parallel}{p} < -\frac{2}{\beta} \Rightarrow \text{firehose instability}, \quad (3)$$

$$\Delta \equiv \frac{p_\perp - p_\parallel}{p} > \frac{1}{\beta} \Rightarrow \text{mirror instability} \quad (4)$$

(the mirror threshold given here is approximate; see Hellinger 2007). These instability conditions are easily achievable in the ICM (see Schekochihin et al. 2005 and references therein). The instabilities are very fast in time and microscopic in space compared to any conceivable macroscopic dynamics because they happen essentially on ion Larmor scales. It is reasonable to expect that their effect will be to keep the plasma locally (at most) marginal with respect to the conditions (3) and (4); solar-wind measurements lend strong support to this expectation (Hellinger et al. 2006; Bale et al. 2009). In order to make that happen, the firehose and mirror fluctuations must impose an upper bound on the effective rate of change of the magnetic field (which gives rise to the pressure anisotropies) and/or increase the effective collisionality of the plasma (which relaxes the anisotropies)—either scenario can lead to macroscopic dynamics dramatically different from the conventional MHD evolution.

This topic was discussed at length (if speculatively) by

Mogavero & Schekochihin (2014), with particular focus on the question of how, under pressure-anisotropic conditions, the magnetic field might be able to grow from a weak primordial seed (believed to be anywhere between 10^{-21} and 10^{-9} G, corresponding to $\beta \sim 10^{32} - 10^8$; see review by Durrer & Neronov 2013) to its observed value ($B \sim 10^6$ G, $\beta \sim 10^2$), even as the rate at which it is allowed to change locally is constrained by the condition

$$\frac{1}{\nu_{\text{eff}}} \frac{1}{B} \frac{dB}{dt} \sim \Delta \equiv \frac{p_\perp - p_\parallel}{p} \in \left[-\frac{2}{\beta}, \frac{1}{\beta} \right], \quad (5)$$

where ν_{eff} is either the Coulomb collision frequency or some effective collisionality determined by particle scattering (if any) off microscopic firehose or mirror fluctuations (see further discussion in section 4.2). This is the question of *plasma dynamo*—magnetogenesis in a weakly collisional turbulent plasma. Besides being of astrophysical (origin of observed fields) and fundamental (what happens?) physical interest, it is likely soon to be attacked not just theoretically, but also experimentally, with the advent of laboratory experiments aiming to reproduce the plasma dynamo process (Spence et al. 2009; Meinecke et al. 2014, 2015; Plihon et al. 2015; Forest et al. 2015). The first demonstration of this process in a 3D kinetic numerical simulation by Rincon et al. (2016) has indeed confirmed the ubiquitous appearance of mirror and firehose fluctuations, although a detailed investigation of the full multiscale problem remains computationally too intensive to be affordable.

There are, obviously, numerous other problems and situations, unrelated to magnetogenesis or to the ICM, in which it matters how a plasma system behaves when it has to effect a local change of the magnetic field. Indeed, in most problems of astrophysical fluid dynamics, the magnetic field and the fluid (plasma) flow are linked, the former being frozen into the latter, and so very little can happen without magnetic field changing under the action of time-dependent velocity gradients.

The type of modelling of the pressure-anisotropy effect on dynamics advocated by Mogavero & Schekochihin (2014) (see also Samsonov et al. 2001; Schekochihin & Cowley 2006; Lyutikov 2007; Kunz et al. 2011), as well as in various numerical implementations of effective closures ensuring that Δ does not stray into the unstable regimes (3) and (4) (Sharma et al. 2006, 2007; Samsonov et al. 2007; Chandran et al. 2011; Meng et al. 2012; Kunz et al. 2012; Santos-Lima et al. 2014), rests on the assumption that, as the magnetic field is locally increased (decreased), the system will stray into mirror (firehose) unstable regimes, instabilities will instantly produce corresponding fluctuations, those will saturate and adjust the instability thresholds (or the system’s position with respect to them). This adjustment is assumed to happen very quickly compared to the time scale on which the system might switch from one instability threshold to the other. Thus, each time such a switch occurs, no memory of previous microscale fluctuations is assumed to be preserved—or, at least, to matter to the macroscopic evolution.

This is certainly a reasonable expectation with regard to triggering the microscale fluctuations: they happen on Larmor timescales, which are always short compared to the time scale on which local macroscale magnetic field changes, because the latter is set by the local shear, rate of strain or

divergence associated with slow, macroscopic motions (we will henceforth refer simply to local shear, but the effect of other types of field-changing motions is analogous). In a turbulent plasma, the local shear time is also the time scale over which the corresponding plasma motion is correlated and so over which a particular local episode of increasing (decreasing) magnetic field will persist. When that ends and the field starts decreasing (increasing) under the influence of a new local shear of, in general, opposite sign and different magnitude, the system is not in fact in a “clean state”—there is a sea of residual microscale fluctuations that were keeping the plasma locally marginal with respect to the old shear. Do they simply decay away to free the system to develop another set of fluctuations suitable for the new shear? Can one, therefore, model macroscopic dynamics in the way that has been emerging in the literature (see above)? This turns out to be a nontrivial question, the answer to which depends on the magnitude of β and has interesting implications for the expected scenario of magnetic-field amplification in astrophysical environments such as the ICM. It is this question that will preoccupy us in this paper and we will show, in particular, that at ultra-high β (very weak fields), plasma develops a persistent multiscale state, with the dynamics of the macroscale fields, pressure anisotropy and microscale (specifically, firehose) fluctuations inextricably linked.

The plan of further proceedings is as follows. In section 2, we will give a brief review of the behaviour of firehose and mirror fluctuations in a shearing plasma and then show how these fluctuations decay when the shear is switched off. The key idea will be that the marginality condition (5) constrains the free decay of microscale turbulence just as it does the rate of change of the magnetic field under shearing. We will also find a new type of driven firehose regime at ultra-high β , in which fluctuations grow for at least a shear time without scattering particles (section 2.1). In section 3, we will investigate what happens when a shear reverses. The most consequential conclusion will be that, at high enough β , switching from decreasing to increasing magnetic field does not cause the system to cross the mirror threshold because of the mitigating effect that residual decaying firehose fluctuations have on the pressure anisotropy (section 3.1.3). In section 4, we will give an itemised summary of our findings (section 4.1) and discuss their implications for the theory of the origin of cosmic magnetism (section 4.2). The conclusions with regard to the latter are broadly optimistic: generally speaking, microphysics does not appear to oppose field growth but is reluctant to allow the field to decay, so the plasma dynamo may be an easier proposition than the MHD one.¹

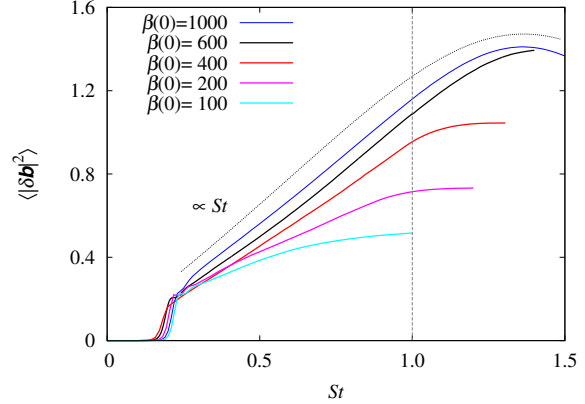


Figure 1. Time evolution of the firehose fluctuation level, $\langle |\delta \mathbf{b}|^2 \rangle$, for runs with $S = 2 \times 10^{-3} \Omega$ and different initial β . The dotted line represents the analytical prediction for secular growth (second line of equation (14), where $\mathbf{B}_0(0)$ is in fact taken at $St = 0.25$, the beginning of the secular-growth stage). Here and in all other plots, $\langle |\delta \mathbf{b}|^2 \rangle = \langle |\delta \mathbf{B}_\perp|^2 \rangle / B_0^2$, including the time dependence of the mean field, $B_0 = B_0(t)$ (see equation (10)).

2 GROWTH, SATURATION AND DECAY OF FIREHOSE AND MIRROR FLUCTUATIONS

2.1 Growth and saturation of firehose fluctuations

2.1.1 Theoretical expectations

Let us start by positing that the mean (ion) pressure anisotropy evolves according to

$$\frac{d\Delta}{dt} = 3 \left\langle \frac{d \ln B}{dt} \right\rangle - 3\nu_{\text{eff}} \Delta. \quad (6)$$

This follows essentially from CGL equations, with account taken of the isotropising effect of collisions (see Schekochihin et al. 2010; Rosin et al. 2011). We have assumed that $p_\perp - p_\parallel \ll p$, that density and temperature do not change with time, that there are no heat fluxes and that ν_{eff} is the larger of the Coulomb collision frequency and the anomalous scattering rate of particles off microscale fluctuations (if any). The angle brackets mean averaging over space (i.e., over the microscales) and we assume that the total magnetic field consists of a slowly decreasing mean field $\mathbf{B}_0 = \langle \mathbf{B} \rangle$ and growing firehose fluctuations $\delta \mathbf{B}_\perp$ (perpendicular to the mean field) excited by the resulting pressure anisotropy. Then, assuming small fluctuations,

$$\langle \ln B \rangle \approx \ln B_0 + \frac{1}{2} \langle |\delta \mathbf{b}|^2 \rangle, \quad \delta \mathbf{b} \equiv \frac{\delta \mathbf{B}_\perp}{B_0}, \quad (7)$$

and equation (6) becomes

$$\frac{1}{3} \frac{d\Delta}{dt} + \nu_{\text{eff}} \Delta = - \left| \frac{d \ln B_0}{dt} \right| + \frac{1}{2} \frac{d \langle |\delta \mathbf{b}|^2 \rangle}{dt}, \quad (8)$$

where we have accentuated the fact that the rate of change of the mean field is negative. In a simple model system where the decrease of the mean field is achieved by persistent linear shear flow $\mathbf{u} = -Sx\hat{\mathbf{y}}$ (Kunz et al. 2014), we have

$$\frac{d \ln B_0}{dt} = - \frac{B_{0x} B_{0y}}{B_0^2} S \equiv -\tilde{S}(t), \quad (9)$$

which is approximately constant in time, $\tilde{S} \sim S$, at times $t \ll S^{-1}$. At longer times, the slow shearing away of the

¹ The idea that plasma dynamo accelerates as the field grows (Schekochihin & Cowley 2006; Mogavero & Schekochihin 2014) appears to have just received some numerical support (Rincon et al. 2016).

mean field,

$$B_0(t) = \sqrt{B_{0x}^2 + [B_{0y}(0) - B_{0x}St]^2}, \quad (10)$$

must be taken into account:

$$\tilde{S}(t) = \frac{B_{0x} [B_{0y}(0) - B_{0x}St]}{B_{0x}^2 + [B_{0y}(0) - B_{0x}St]^2} S. \quad (11)$$

Assuming further that the system (after an initial transient) will settle into a marginal state,

$$\Delta \rightarrow -\frac{2}{\beta}, \quad (12)$$

we find from equation (8) that in such a state,

$$-\frac{2\nu_{\text{eff}}}{\beta} = -\tilde{S} + \frac{1}{2} \frac{d\langle |\delta \mathbf{b}|^2 \rangle}{dt} \quad (13)$$

(we assume $\beta \gg 1$ and so the $d\Delta/dt$ term is small). In a driven system where B_0 is continuously decreased, the marginality (13) can be achieved in two ways. In the absence of anomalous scattering ($\nu_{\text{eff}} \ll S\beta$), the rate of growth of the total energy of the firehose fluctuations can cancel the rate of decrease of the mean field, leading to secularly growing “firehose turbulence” (Schekochihin et al. 2008; Rosin et al. 2011):

$$\begin{aligned} \frac{1}{2} \langle |\delta \mathbf{b}|^2 \rangle(t) &= \int_0^t dt' \tilde{S}(t') \\ &= \ln \left[1 - \frac{2B_{0y}(0)B_{0x}}{B_0^2(0)} St + \frac{B_{0x}^2}{B_0^2(0)} (St)^2 \right]^{-1/2} \\ &\sim St. \end{aligned} \quad (14)$$

Alternatively, if the firehose fluctuations are capable of scattering particles, they can happily saturate provided the scattering rate satisfies

$$\nu_{\text{eff}} = \frac{\tilde{S}\beta}{2} \sim S\beta. \quad (15)$$

Which of these effects takes precedence in reality?

2.1.2 Numerical results

The numerical study by Kunz et al. (2014) has shown that both of these scenarios do occur, sequentially: in their simulations, after a period of secular growth obeying equation (14) and no particle scattering, the (oblique) firehose turbulence developed an effective collisionality very close to that given by equation (15) and saturated at a level that scaled as² $\langle |\delta \mathbf{b}|^2 \rangle \propto S^{1/2}$. However, these simulations were all done at one value of (initial) beta $\beta(0) = 200$. In what follows, the β dependence of the saturated state will matter and so we now extend the Kunz et al. (2014) parameter study to a range $\beta(0) \in [100, 1000]$.

We use the same set up and the same code as Kunz et al. (2014) and carry out a series of hybrid (kinetic ions, isothermal electrons), δf PIC simulations of a collisionless plasma in a 2D box where an initial magnetic field in the (x, y) plane (with $B_{0x} > 0$, $B_{0y}(0) > 0$) is slowly reduced by linear shearing as per equation (9) with $S > 0$. The numerical details are documented in appendix A.

² There is currently no theoretical understanding of this scaling.

We find that firehose fluctuations grow secularly according to equation (14) (figure 1) until they saturate at a level that scales with both S and β , a new result:

$$\langle |\delta \mathbf{b}|^2 \rangle \sim \left(\beta \frac{S}{\Omega} \right)^{1/2} \quad (16)$$

(see figure 2a). This scaling can of course only be valid provided the resulting fluctuation level is small (< 1). At sufficiently high β and/or S , viz., such that

$$\beta \gtrsim \frac{\Omega}{S}, \quad (17)$$

this is no longer true and $\langle |\delta \mathbf{b}|^2 \rangle$ saturates at an order-unity level independent of either β or S . Whereas the secularly growing firehose fluctuations do not scatter particles, the saturated ones do, at a rate that scales with $S\beta$ in a manner consistent with equation (15) (figure 2b; how the effective collisionality is calculated is explained in appendix A5).

Clearly, when $\beta \ll \Omega/S$, reaching saturation requires only a fraction of the shear time:

$$\langle |\delta \mathbf{b}|^2 \rangle \sim St_{\text{sat}} \sim \left(\frac{\beta S}{\Omega} \right)^{1/2} \Rightarrow t_{\text{sat}} \sim \left(\frac{\beta}{S\Omega} \right)^{1/2} \ll S^{-1}. \quad (18)$$

In this limit, since typically local shears in a macroscopic plasma flow will change in time at the rates comparable to those shears themselves, one can safely consider the anomalous collisionality associated with the firehose fluctuations to turn on instantaneously, in line with the macroscopic modeling assumption that we discussed in section 1. This, however, is no longer the case when $\beta \gtrsim \Omega/S$, as it takes $t_{\text{sat}} \sim S^{-1}$ to reach a finite $\langle |\delta \mathbf{b}|^2 \rangle$ and for the fluctuations to start scattering particles. Thus, at these “ultra-high” betas, the firehose fluctuations grow secularly during much of the shear time, approximately conserve μ and do not scatter particles efficiently.³ The implications of this will be discussed in sections 3.1 and 4.2.1.

Figures 3a and 3b show snapshots of the firehose fluctuation field for $\beta(0) = 600$ and $S/\Omega = 2 \times 10^{-3}$ during the period of secular growth ($St = 0.4$, figure 3a), when the fluctuations do not scatter particles efficiently, and later in the evolution ($St = 1.0$, figure 3b), when the scattering becomes significant (see figure 4a, which documents the evolution of both $\langle |\delta \mathbf{b}|^2 \rangle$ and ν_{eff} for the same run). While precisely what happens in this later stage is not well understood, it may be a useful observation that the firehose structures appear to start shredding—perhaps a sign of nonlinear interactions of hydrodynamic (advective), rather than quasilinear type (the latter is what controls the secular regime; see Rosin et al. 2011). Small, Larmor and sub-Larmor, scales that are produced this way should be more efficient at scattering particles.

2.2 Free decay of firehose turbulence

Let us now consider what happens if we start in a state that is firehose-marginal, with firehose fluctuations that have

³ Note that when they saturate and do start scattering particles (provided they ever reach saturation), the effective collision rate (15) needed to maintain the plasma at the firehose threshold is larger than the cyclotron frequency, and so the plasma becomes effectively unmagnetised.

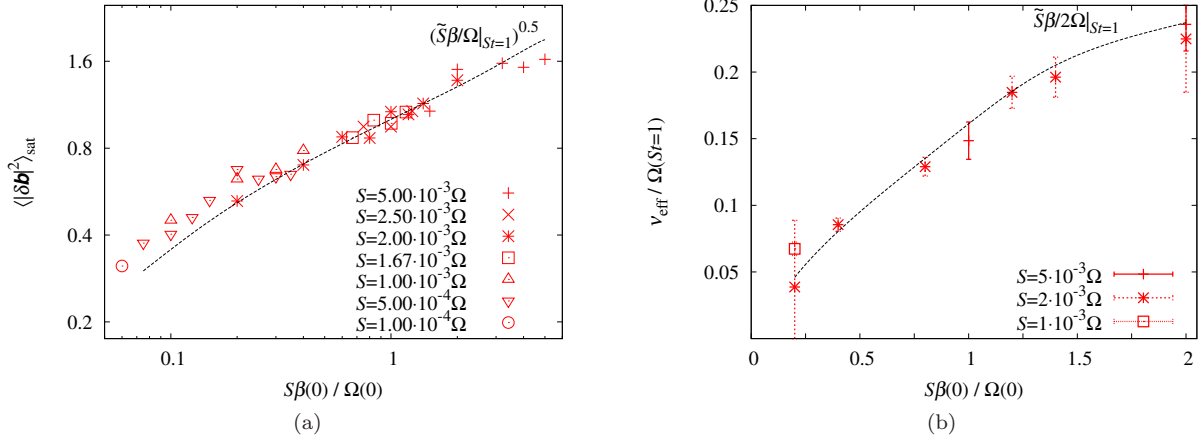


Figure 2. Dependence of (a) the saturated level of driven firehose fluctuations $\langle |\delta \mathbf{b}|^2 \rangle$ and (b) their effective scattering rate ν_{eff}/Ω (calculated by the method described in appendix A5) on shear S and plasma beta β . The dotted line in (a) is the empirical scaling (16), including a fitting constant and using the value of β at $St = 1$: $\langle |\delta \mathbf{b}|^2 \rangle \approx 0.77(\beta\tilde{S}/\Omega)^{1/2}$, where \tilde{S} is defined in equation (9). This scaling is not theoretically understood, but manifestly quite well satisfied except when $\beta \gtrsim \Omega/S$. The dotted line in (b) is the theoretical value (15) required for the anomalous scattering to pin the anisotropy at marginal level (where it is indeed pinned; see figure 4b).

been secularly growing for one shear time, $St = 1$ (and, depending on β , might have saturated), and remove the drive, i.e., switch off the shear (in section 3, we will “generalise” this to reversing the shear rather than switching it off). How fast will the fluctuations decay?

2.2.1 Theoretical expectations

To answer this question, one must realise that decaying fluctuations imply decreasing mean magnetic energy, which by itself can drive negative mean pressure anisotropy, pushing the system towards an unstable state. It is then reasonable to argue that the rate of decay of the firehose turbulence should not exceed the marginal level set by equation (13), but with the mean field no longer changing, $d \ln B_0/dt = -\tilde{S} = 0$:

$$\frac{1}{2} \frac{d\langle |\delta \mathbf{b}|^2 \rangle}{dt} = -\frac{2\nu_{\text{eff}}}{\beta}. \quad (19)$$

Physically, the negative pressure anisotropy generated by the decay of the initial fluctuations should in turn generate new firehose fluctuations, slowing down the decay to the marginal level.⁴

The anomalous collisionality ν_{eff} is itself obviously a function of the magnitude of the fluctuations. The simplest (even perhaps simplistic) way to estimate this dependence is as follows. Consider a gyrating particle streaming along a perturbed field line whose parallel scale length is l_{\parallel} . In the limit $l_{\parallel} \gg \rho_i$, i.e., when the perturbations decorrelate on parallel scales much longer than the Larmor radius $\rho_i = v_{\text{th}}/\Omega$ and, therefore, as the particle travels the

distance $\sim v_{\text{th}}/\Omega$ during one Larmor period, the magnetic field it sees remains unchanged, the first adiabatic invariant $\mu = v_{\perp}^2/B$ is conserved with exponential precision for each particle (Kruskal 1958). In contrast, if $l_{\parallel} \sim \rho_i$ (as it indeed is for the fastest-growing oblique firehose perturbations; see Kunz et al. 2014), particle orbits fail to close precisely on themselves and a particle’s perpendicular momentum, or, equivalently, its μ , suffers a random change over each Larmor period $\delta t \sim \Omega^{-1}$:

$$\frac{\Delta \mu}{\mu} \sim \frac{\Delta v_{\perp}}{v_{\perp}} \sim \frac{\delta F \delta t}{mv_{\perp}} \sim \frac{\delta B_{\perp}}{B_0}, \quad (20)$$

where $\delta F \sim ev_{\perp} \delta B_{\perp}/c = mv_{\perp} \Omega \delta B_{\perp}/B_0$ is the perturbed Lorentz force on the particle.⁵ Assuming diffusive accumulation of these changes—essentially, pitch-angle diffusion—the diffusion coefficient is the effective collisionality of the plasma permeated by firehose fluctuations:

$$\nu_{\text{eff}} \sim \frac{\langle (\Delta \mu/\mu)^2 \rangle}{\Delta t} \sim \Omega \langle |\delta \mathbf{b}|^2 \rangle, \quad (21)$$

where $\Delta t \sim l_{\parallel}/v_{\text{th}} \sim \rho_i/v_{\text{th}} = \Omega^{-1}$ is the time for the particle to transit through one correlation length of the firehose turbulence and so the time between random kicks of the size given by equation (20).

Using equation (21) and ignoring the slow time dependence of β and Ω due to changing total B , we infer from equation (19) an exponential decay of the firehose fluctuations:

$$\langle |\delta \mathbf{b}|^2 \rangle \propto e^{-\gamma t}, \quad \gamma \sim \frac{\Omega}{\beta}. \quad (22)$$

2.2.2 Numerical results

Remarkably, this simple argument appears to describe quite well what happens in the following numerical experiment.

⁴ A disclaimer is in order. Equations (13), (19) and similar ones in what follows should not be taken as precise statements: technically speaking, they can only be derived as controlled approximations if the scale of the firehose fluctuations is large compared to the Larmor scale (Rosin et al. 2011). In reality, their scale is of the same order as the ion Larmor scale (Kunz et al. 2014), which is why they are able to scatter particles. As we will see in analysing our numerical experiments below, the β scalings that we obtain in this non-rigorous way are nevertheless correct.

⁵ There is also a contribution to $\delta \mu/\mu$ due to the variation in the field strength, but for firehose perturbations, this is second-order, $\delta B/B_0 \sim \delta B_{\perp}^2/B_0^2$ (see equation (7)), and so can be ignored here.

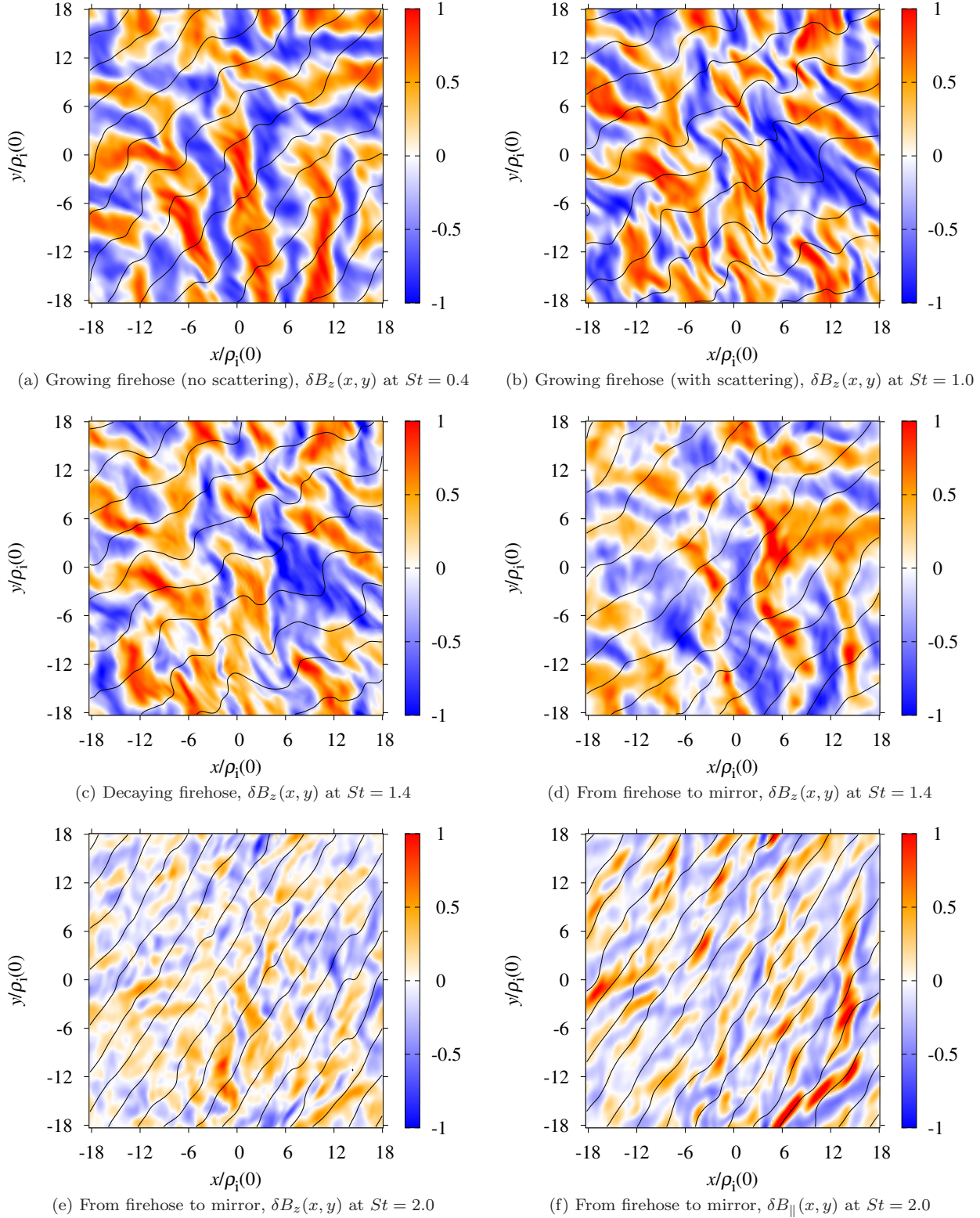


Figure 3. A series of snapshots of the fluctuating fields in simulations with $\beta(0) = 600$ and $S = 2 \times 10^{-3}\Omega$, starting in the firehose-unstable regime: (a) $\delta B_z(x, y)$ (proxy for $\delta \mathbf{B}_\perp$) at $St = 0.4$ (growing firehose perturbations, no anomalous scattering; see figure 4a and d); (b) same as (a) at $St = 1.0$ (growing firehose perturbations, but now with substantial anomalous scattering; see figure 4a and d); (c) same as (b) at $St = 1.4$ in a run where shear was switched off at $St = 1$ (decaying firehose perturbations; see figure 4a); (d) same as (b) at $St = 1.4$ in a run where shear was reversed at $St = 1$ (firehose perturbations being sheared away; see figure 11a); (e) same as (d) at $St = 2.0$ in the run with reversed shear (firehose perturbations are nearly gone; see figure 11a); (f) $\delta B_{||}(x, y)$ in the same run and at the same time as (e) (mirror perturbations starting to grow; see figure 11a). The x and y coordinates are shown in the units of the ion Larmor radius at the start of the simulation, $\rho_i(0)$. Black lines are magnetic-field lines.

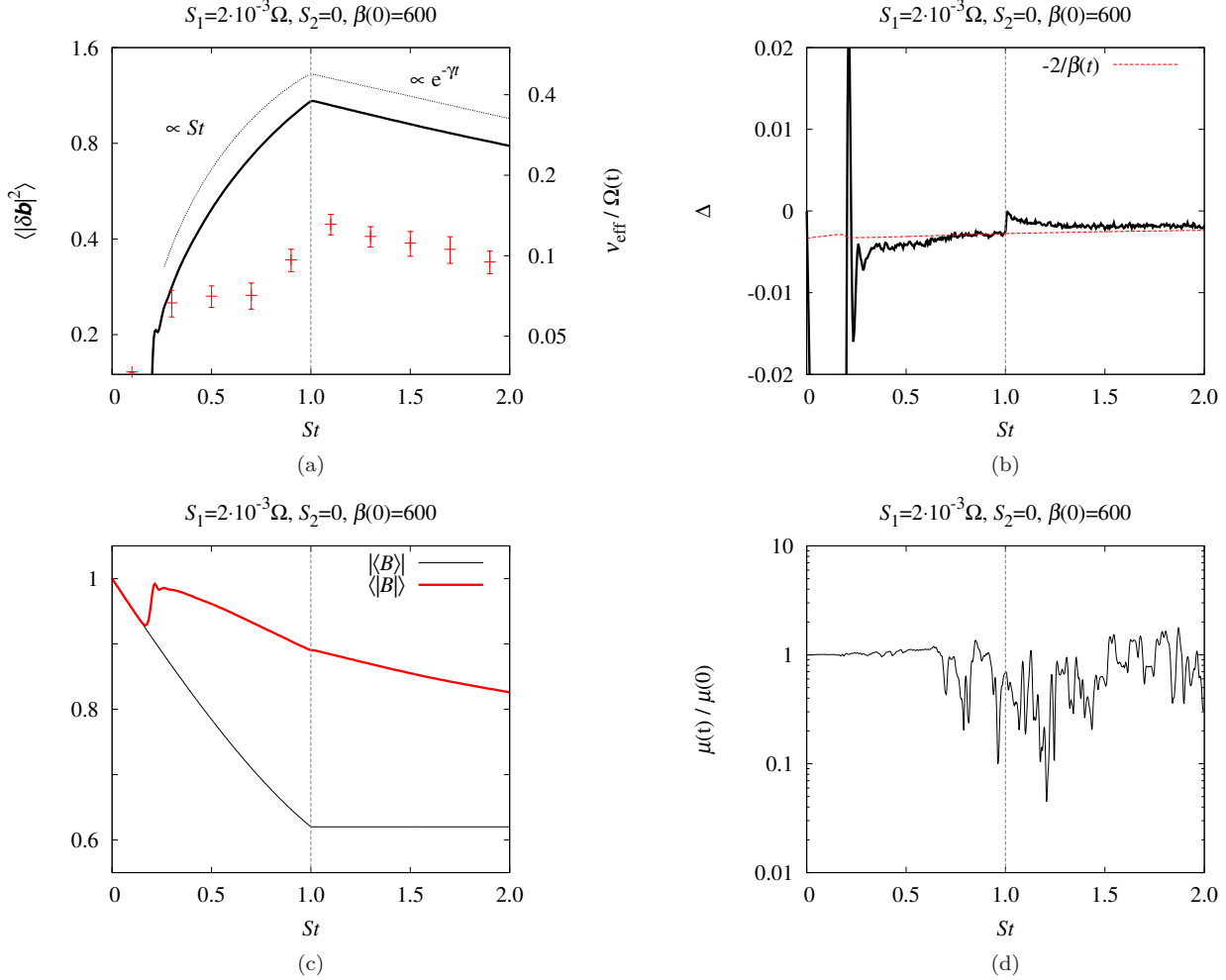


Figure 4. Time history of the numerical experiment described in section 2.2, starting with a shear that decreases the mean field and then switching it off after one shear time, $St = 1$. In the particular case shown here, the initial shear was $S = 2 \times 10^{-3} \Omega$ and $\beta(0) = 600$, so this case is marginal with respect to the change of physical regime at $\beta \sim \Omega/S$. (a) Black solid line: time evolution of $\langle |\delta \mathbf{b}|^2 \rangle$. The dotted line at $St < 1$: the analytical estimate for secular growth (second line of equation (14), where $\mathbf{B}_0(0)$ is in fact taken at $St = 0.25$, the beginning of the secular-growth stage). The dotted line at $St > 1$: the slope corresponding to the exponential decay at the rate $\gamma = 0.9\Omega/\beta$ (calculated at $St = 1$), consistent with equation (22). Red crosses: the effective collisionality ν_{eff}/Ω , calculated by the method described in appendix A5 (numerical values are shown on the vertical axis on the right of the plot). During secular growth, ν_{eff} starts increasing when the fluctuation level approaches $\langle |\delta \mathbf{b}|^2 \rangle \sim 1$. During the decay, ν_{eff} manifestly follows $\langle |\delta \mathbf{b}|^2 \rangle$, in agreement with equation (21). (b) Time evolution of the pressure anisotropy $\Delta = (p_{\perp} - p_{\parallel})/p$. Red dotted line shows the marginal level, $\Delta = -2/\beta(t)$ (this includes the slow increase of β with time during the sheared stage). The firehose turbulence is near-marginal in all nonlinear growth and decay stages. (c) Time evolution of the mean-field magnitude, $B_0 = |\langle \mathbf{B} \rangle|$ (black thin line) and of the mean magnitude of the field, $\langle B \rangle = \langle |\mathbf{B}| \rangle$ (red bold line). (d) Time evolution of the first adiabatic invariant $\mu = v_{\perp}^2/B$ for a single particle: μ is initially conserved during secular growth, but this conservation is broken as fluctuations become large, $\langle |\delta \mathbf{b}|^2 \rangle \sim 1$, and continues to be broken during the decay of the firehose turbulence.

For a number of values of S and initial beta $\beta(0)$, we first run the same simulations as described in section 2.1 for one shear time; as we explained there, for $\beta \ll \Omega/S$, this is long enough to obtain saturated, particle-scattering firehose turbulence in the marginal state (12), whereas for $\beta \gtrsim \Omega/S$, the firehose turbulence with $\langle |\delta \mathbf{b}|^2 \rangle \sim 1$ is just about formed after one shear time (the subsequent evolution that we are about to describe is the same in both regimes). Then we switch off the shear and allow the fluctuations to decay. This time history is shown in figure 4 for a representative run (see figure 3a–c for snapshots of the firehose fluctuation field for

this run at stages 2, 3 and 4 described below). The system goes through the following stages of evolution:

1. initial, linear growth of firehose fluctuations as the pressure anisotropy, starting from zero, crosses the threshold (3), overshoots...
2. ...and is then returned to the marginal level (12) as linear growth of fluctuations gives way to secular growth, according to equation (14); there is no particle scattering until...
3. ...the fluctuation energy approaches the level given by

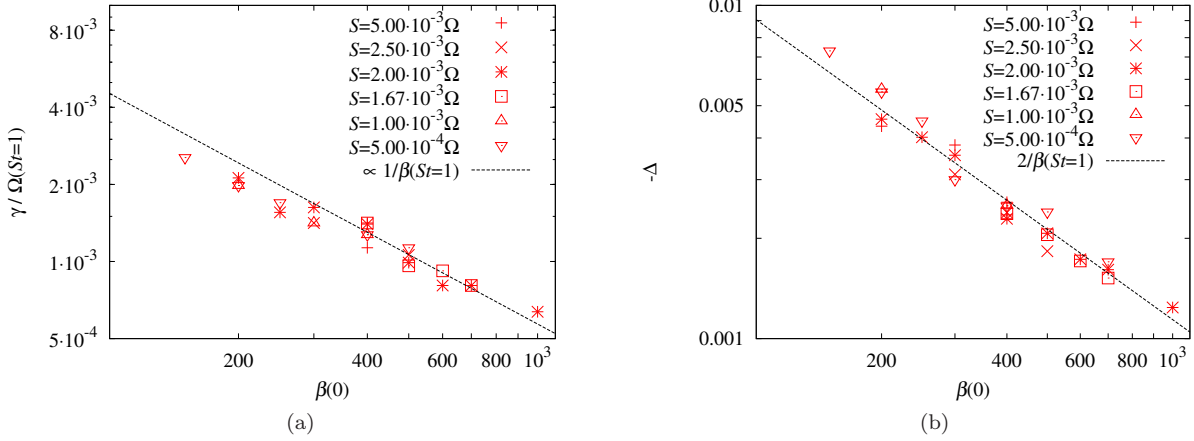


Figure 5. (a) Decay exponent γ/Ω for the firehose turbulence (section 2.2) vs. $\beta(0)$, at various values of initial S (on which it manifestly does not depend). The fit $\gamma = \Omega/\beta(St = 1)$ is shown as a dotted line and is manifestly a good description of the data, confirming equation (22). (b) Mean (negative) pressure anisotropy $-\Delta = (p_{\parallel} - p_{\perp})/p$ for the same decaying runs. The firehose-marginal level, $-\Delta = 2/\beta(St = 1)$, is shown as a dotted line, confirming that decaying firehose turbulence stays marginal, as argued in section 2.2.

equation (16) or by $\langle |\delta \mathbf{b}|^2 \rangle \sim 1$ if $\beta \gtrsim \Omega/S$, giving rise to $\nu_{\text{eff}} \sim S\beta$, as per equation (15);⁶

4. the shear is switched off at $St = 1$ and fluctuations decay exponentially, at a rate given by equation (22); during this decay, the effective collisionality ν_{eff} scales with $\langle |\delta \mathbf{b}|^2 \rangle$ according to equation (21), while the pressure anisotropy stays firehose-marginal.⁷

Figure 5a confirms that the decay rate scales with β according to equation (22) and is independent of the initial shear S for a number of values of these parameters. Figure 5b confirms that the pressure anisotropy (which is approximately constant in the decay stage of all these runs) always stays at the firehose-marginal level (12). Finally, figure 6 shows that the effective collisionality scales with $\langle |\delta \mathbf{b}|^2 \rangle$ as predicted by equation (21) at all values of S and β and also at various times during the decay.

2.3 Growth and saturation of mirror fluctuations

Let us now consider what happens when the mean field is locally increased, rather than decreased, driving the system through the mirror threshold (4). Compared to the firehose, this is an analytically more complicated situation, a careful treatment of which can be found in Rincon et al. (2015).

⁶ In the ultra-high- β regime, while the onset of anomalous scattering occurs as the fluctuation level approaches unity, $\langle |\delta \mathbf{b}|^2 \rangle \sim 1$, this does not stop $\langle |\delta \mathbf{b}|^2 \rangle$ from continuing to increase (although this increase is partly due to $B_0(t)$ decreasing slowly, as we have defined $\langle |\delta \mathbf{b}|^2 \rangle = \langle |\delta \mathbf{B}_{\perp}|^2 \rangle / B_0^2(t)$ with respect to the time-dependent mean field).

⁷ Note that when the shear is switched off, the anisotropy first relaxes very quickly to zero (see figure 4b). The time scale on which this happens is consistent with the collision time associated with the firehose fluctuations at that moment: from figure 4a, $S/\nu_{\text{eff}} \sim 0.01$. The subsequent return to a firehose-marginal state occurs from the stable side (i.e., $\Delta \rightarrow -2/\beta$ from above). This means that the decaying firehose fluctuations, unlike the driven ones, have some similarity to propagating Alfvén waves, albeit with reduced phase speed (cf. Kunz et al. 2015).

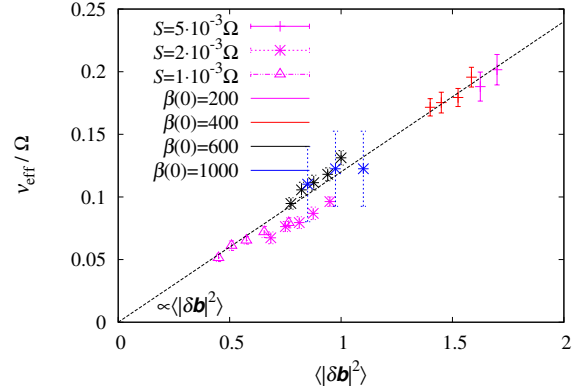


Figure 6. Effective collisionality ν_{eff}/Ω vs. mean square fluctuation level $\langle |\delta \mathbf{b}|^2 \rangle$ at various times during the decay stage of the firehose turbulence (section 2.2) and at various values of initial S and β . The dotted line shows the fit $\nu_{\text{eff}}/\Omega = 0.15 \langle |\delta \mathbf{b}|^2 \rangle$, consistent with the scaling (21) and manifestly a good description of the data.

Here, we will give a vulgarised qualitative discussion, at the risk of outraging a purist reader, but hopefully with the benefit of enlightening an impatient one.

Let us continue using equation (6) to describe the evolution of the mean pressure anisotropy, except the angle averaging will now mean averaging over particle trajectories. For passing particles, this is the same as spatial averaging, but, in the case of mirror fluctuations, there will also be a population of particles trapped in these fluctuations—for these particles, the average that matters in the calculation of the pressure anisotropy is the bounce average (Rincon et al. 2015). The mirror fluctuations are, to lowest order in their amplitude, fluctuations of the magnetic-field strength, or δB_{\parallel} (a snapshot showing what they look like is given in figure 7a for a run with the same parameters as the firehose run in figure 3, but with the opposite sign of the shear).

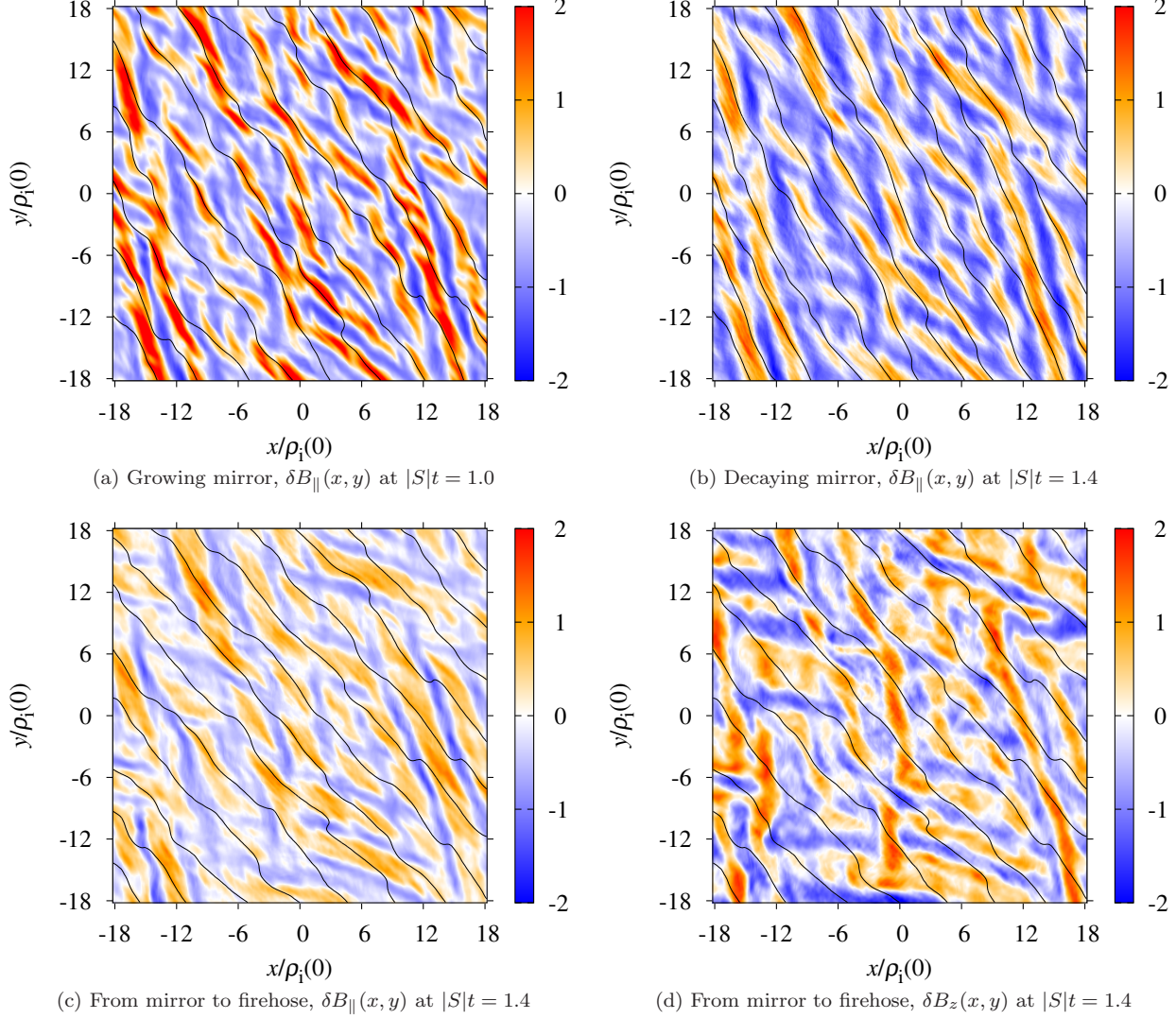


Figure 7. A series of snapshots of the fluctuating fields in simulations with $\beta(0) = 600$ and $S = -2 \times 10^{-3}$, starting in the mirror-unstable regime: (a) $\delta B_{\parallel}(x, y)$ at $|S|t = 1.0$ (growing mirror perturbations; see figure 8a and d); (b) same as (a) at $|S|t = 1.4$ in a run where shear was switched off at $|S|t = 1$ (decaying mirror perturbations; see figure 8a); (c) same as (a) at $|S|t = 1.4$ in a run where shear was reversed at $|S|t = 1$ (mirror perturbations being sheared away; see figure 12a); (f) $\delta B_z(x, y)$ (proxy for δB_{\perp}) in the same run and at the same time as (c) (growing firehose perturbations; see figure 12a). The x and y coordinates are shown in the units of the ion Larmor radius at the start of the simulation, $\rho_i(0)$. Only the central $36 \times 36 \rho_i^2(0)$ patch of a larger $82 \times 82 \rho_i^2(0)$ simulation box is shown, for comparison with figure 3. Black lines are magnetic-field lines. Note that the range of amplitudes is large, $\delta B_{\parallel} \in [-2, 2]$, because they are normalised to the initial field (whereas the mean field $B_0(t)$ grows with time at $|St| \leq 1$).

Therefore,

$$\langle \ln B \rangle \approx \ln B_0 + \left\langle \frac{\delta B_{\parallel}}{B_0} \right\rangle \sim \ln B_0 - \left| \frac{\delta B_{\parallel}}{B_0} \right|^{3/2}, \quad (23)$$

where the last, qualitative, estimate is based on the expectation that the only non-zero contribution to $\langle \delta B_{\parallel} \rangle$ will come from the trapped particles, that it is negative because the trapped particles are trapped in areas of smaller B , and that the fraction of these particles in the system is $\sim |\delta B_{\parallel}/B_0|^{1/2}$. Assuming that the pressure anisotropy will tend to marginal,

$$\Delta \rightarrow \frac{1}{\beta}, \quad (24)$$

the analogue of equation (13) for the mirror is (non-

rigorously)

$$\frac{d \ln B_0}{dt} - \frac{d}{dt} \left| \frac{\delta B_{\parallel}}{B_0} \right|^{3/2} \sim \frac{\nu_{\text{eff}}}{\beta}. \quad (25)$$

Again, in view of equation (9), there is a secular growth regime (Schekochihin et al. 2008),

$$\left| \frac{\delta B_{\parallel}}{B_0} \right| \sim (|S|t)^{2/3}, \quad (26)$$

assuming inefficient scattering of particles by mirror modes ($\nu_{\text{eff}} \ll S\beta$) and so an approximate balance in the left-hand side of equation (25) (for the rigorous derivation of this secular evolution, see Rincon et al. 2015).

This is indeed what happens for much of the nonlinear evolution of the mirror instability (Kunz et al. 2014). Physically, just like the firehose fluctuations in the secular-growth

regime combined to compensate on average for the decline of the mean field and thus allow the particles to conserve their μ , the mirror fluctuations accomplish a similar feat but by a different ruse: as the mean field grows, an increasing number of particles gets trapped in increasingly deep mirrors, protecting those particles from the effect the growing field would have had on their μ (cf. Kivelson & Southwood 1996; Pantellini 1998; Pokhotelov et al. 2008; Rincon et al. 2015). Thus, whereas both $|\langle \mathbf{B} \rangle|$ and $\langle |\mathbf{B}| \rangle$ grow in the volume-averaged sense, $\langle |\mathbf{B}| \rangle$ does *not* grow if averaged over particle trajectories. Figure 8c documents the time evolution of both the volume-averaged (mean) field $|\langle \mathbf{B} \rangle|$ and the volume-averaged total field strength $\langle |\mathbf{B}| \rangle$ during such a secular stage (at $|S|t < 1$). Unlike in the case of the decaying mean field (figure 4c), where the secular growth of the firehose fluctuations slowed down the rate of decay of the total field strength, the mirror fluctuations do not decrease the rate of the total field's growth. This is because marginal pressure anisotropy is achieved by rearranging particles between the passing and trapped populations, rather than by impeding the change of B .⁸

Scattering is small in this regime (see figures 8a and d at $St < 1$, and more asymptotic cases with lower S in Kunz et al. 2014) because both linear and nonlinear mirror modes near the threshold are quite well separated from the Larmor scale (Hellinger 2007; Rincon et al. 2015) and thus conserve μ ; a significant ν_{eff} is only achieved after the mirror turbulence saturates at

$$\left| \frac{\delta B_{\parallel}}{B_0} \right| \sim 1, \quad (27)$$

independently of S (Kunz et al. 2014; Riquelme et al. 2015), with scattering likely occurring at sharp (Larmor-scale) boundaries of the mirror wells. The time to saturation is $St \sim 1$ and so the secular regime should be the relevant one most of the time during each episode of the mean-field growth.

2.4 Free decay of mirror turbulence

2.4.1 Theoretical expectations

Just as we did for the firehose case, we now ask what happens if we switch off the shear at $St = 1$. The mirrors must start decaying and, as they decay, more and more of the particles previously trapped in them are released. As these particles escape the mirrors, they are able to sample regions of stronger field and so, as far as the particles are concerned, they, on average, see an *increasing* field and so the pressure anisotropy will be pushed upwards! This seemingly paradoxical conclusion is made more intuitive by noting that the net effect of the secularly growing mirror fluctuations in the driven regime described in section 2.3 was to push the pressure anisotropy down; now that these mirror fluctuations decay, the anisotropy will go back up. As it is limited from above by the mirror instability threshold, it is natural to assume (analogously to what we did in section 2.2) that the

decaying mirror turbulence will stay in the marginal state (24). With the drive (growing B_0) removed, equation (25) becomes

$$-\frac{d}{dt} \left| \frac{\delta B_{\parallel}}{B_0} \right|^{3/2} \sim \frac{\nu_{\text{eff}}}{\beta}. \quad (28)$$

The effective collisionality ν_{eff} can be estimated by assuming that the breaking of μ conservation will happen as particles encounter sharp edges of saturated mirrors (Kunz et al. 2014). By the argument that led to equation (20), the relative change in μ resulting from such an encounter is

$$\frac{\Delta\mu}{\mu} \sim \Omega \delta t \frac{\delta B_{\perp}}{B_0} \sim \Omega \delta t \frac{l_{\perp}}{l_{\parallel}^{(\text{edge})}} \left| \frac{\delta B_{\parallel}}{B_0} \right|, \quad (29)$$

where δt is the time the particle takes to transit the sharp-edge region, which must be shorter than the cyclotron period, $\Omega \delta t \lesssim 1$ (otherwise μ will be conserved with exponential precision; see Kruskal 1958). The second expression in equation (29) was obtained by using solenoidality of the magnetic field to estimate the perpendicular perturbation of the magnetic field in a mirror's edge in terms of its parallel perturbation; l_{\perp} is the perpendicular scale of the mirror and $l_{\parallel}^{(\text{edge})}$ is the parallel extent of its edge. If v_{\parallel} is the parallel velocity of the particle, then $\delta t \sim l_{\parallel}^{(\text{edge})}/v_{\parallel}$ and we get⁹

$$\frac{\Delta\mu}{\mu} \sim \frac{l_{\perp}}{\rho_i} \left(\frac{v_{\parallel}}{v_{\text{th}}} \right)^{-1} \left| \frac{\delta B_{\parallel}}{B_0} \right|. \quad (30)$$

The prefactor $(v_{\parallel}/v_{\text{th}})^{-1} \sim 1$ for the passing particles and $(v_{\parallel}/v_{\text{th}})^{-1} \sim |\delta B_{\parallel}/B_0|^{-1/2}$ for the trapped ones; the latter suffer a bigger change in μ because they take longer to transit the edge region. Note that the condition $\Omega \delta t \lesssim 1$ implies that the scale of the sharp region should be

$$l_{\parallel}^{(\text{edge})} \lesssim \left| \frac{\delta B_{\parallel}}{B_0} \right|^{1/2} \rho_i \quad (31)$$

for the trapped particles to be scattered, enabling the mirror modes to saturate at the end of their driven stage.

Assuming again that the kicks to μ given by equation (30) accumulate diffusively, the pitch-angle diffusion coefficient, or the effective collisionality of the plasma permeated by mirrors, is

$$\begin{aligned} \nu_{\text{eff}} &\sim \frac{\langle (\Delta\mu/\mu)^2 \rangle}{\Delta t} \sim \frac{(l_{\perp}/\rho_i)^2}{l_{\parallel}^{(\text{mirror})}/\rho_i} \Omega \left(\frac{v_{\parallel}}{v_{\text{th}}} \right)^{-1} \left| \frac{\delta B_{\parallel}}{B_0} \right|^2 \\ &\sim \Omega \left(\frac{v_{\parallel}}{v_{\text{th}}} \right)^{-1} \left| \frac{\delta B_{\parallel}}{B_0} \right|^2. \end{aligned} \quad (32)$$

To obtain this estimate, we have used equation (30) and assumed that the time between random kicks of the size given by it is the time for the particles to transit the full length $l_{\parallel}^{(\text{mirror})}$ of a mirror, $\Delta t \sim l_{\parallel}^{(\text{mirror})}/v_{\parallel}$ (for the trapped particles, this is the bounce time). The final expression in equation (32) follows if we also assume that we can use for the nonlinear mirrors (Kunz et al. 2014; Rincon et al. 2015)

⁸ Note that this means that the upper bound on the growth rate of B conjectured by Mogavero & Schekochihin (2014, §3) is likely to have been too pessimistic (see updated discussion in section 4.2).

⁹ The contribution to $\Delta\mu$ due to the change in the denominator of $\mu = v_{\perp}^2/B$, $\Delta\mu/\mu \sim |\delta B_{\parallel}/B_0|$, is always smaller than that given by equation (30) because $l_{\perp} \gg \rho_i$ for near-marginal mirrors (Hellinger 2007; Rincon et al. 2015).

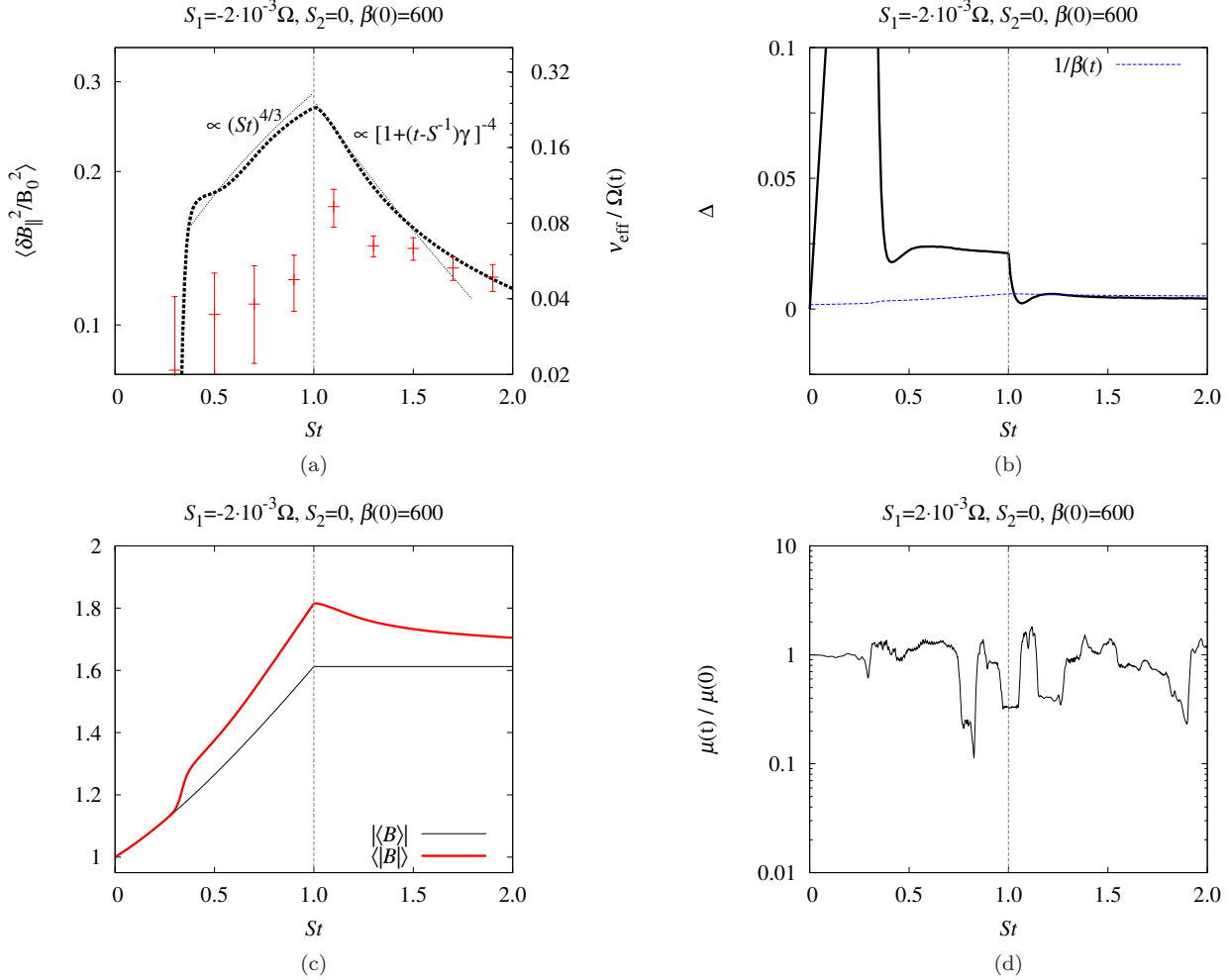


Figure 8. Same as figure 4, but starting with negative shear, $S = -2 \times 10^{-3} \Omega$, and so increasing the mean magnetic field. Same quantities are shown, with the following differences. (a) Time evolution of the mirror perturbations, $\langle \delta B_{\parallel}^2 / B_0^2 \rangle$ is shown by the bold black dotted line; time-dependent mean field $B_0(t)$ is used for normalisation. Dotted lines show the theoretical estimates for the secular growth of driven mirror turbulence at $|S|t < 1$, equation (26), and for the decay of the decaying one at $|S|t > 1$, equation (37) (with $t_0 = |S|^{-1}$ and $\gamma = 0.19\Omega/\beta$, calculated at $St = 1$; note that the label in the plot omits the factor of $[\langle \delta B_{\parallel}^2 / B_0^2 \rangle(t_0)]^{1/4}$ in front of γ for lack of space, but this factor is present in the fit). (b) Blue dotted line shows the marginal level of pressure anisotropy for the mirror instability, $\Delta = 1/\beta(t)$. (d) The first adiabatic invariant $\mu = v_{\perp}^2/B$ is conserved throughout the sheared stage.

the result that $l_{\parallel}^{(\text{mirror})}/\rho_i \sim (l_{\perp}/\rho_i)^2 \sim (\beta\Delta - 1)^{-1}$ for the fastest growing linear mirror modes (Hellinger 2007). Finally, letting $v_{\parallel}/v_{\text{th}} \sim 1$ for the passing particles and $v_{\parallel}/v_{\text{th}} \sim |\delta B_{\parallel}/B_0|^{1/2}$ for the trapped ones, we arrive at

$$\nu_{\text{eff}}^{(\text{trapped})} \sim \Omega \left| \frac{\delta B_{\parallel}}{B_0} \right|^{3/2}, \quad (33)$$

$$\nu_{\text{eff}}^{(\text{passing})} \sim \Omega \left| \frac{\delta B_{\parallel}}{B_0} \right|^2. \quad (34)$$

The trapped particles are scattered more vigorously.

Since equation (28) was deduced (non-rigorously) by accounting for the bounce-averaged contribution of the trapped particles to the pressure anisotropy (see equation (6) and section 2.3), we should use the effective collisionality of the trapped population.

The effective collisionality that appears in equation (28) is the rate of relaxation of pressure anisotropy, to which the scattering of both trapped and passing particles con-

tributes. Therefore, the total collisionality must be an average of $\nu_{\text{eff}}^{(\text{trapped})}$ and $\nu_{\text{eff}}^{(\text{passing})}$ weighted by the fraction of each type of particles. Since the fraction of trapped particles is $\sim |\delta B_{\parallel}/B_0|^{1/2}$, this weighted average is

$$\nu_{\text{eff}} \sim \Omega \left| \frac{\delta B_{\parallel}}{B_0} \right|^2. \quad (35)$$

Substituting this formula into equation (28), we get

$$\frac{d}{dt} \left| \frac{\delta B_{\parallel}}{B_0} \right|^{3/2} \sim -\gamma \left| \frac{\delta B_{\parallel}}{B_0} \right|^2, \quad \gamma \sim \frac{\Omega}{\beta}. \quad (36)$$

The solution for the mean square mirror fluctuation is

$$\left\langle \frac{\delta B_{\parallel}^2}{B_0^2} \right\rangle(t) = \frac{\langle \delta B_{\parallel}^2 / B_0^2 \rangle(t_0)}{\left\{ 1 + (t - t_0)\gamma \left[\langle \delta B_{\parallel}^2 / B_0^2 \rangle(t_0) \right]^{1/4} \right\}^4}, \quad (37)$$

where t_0 is the time at which free decay starts, in our case $t_0 = |S|^{-1}$. Thus, mirrors decay on the same time scale \sim

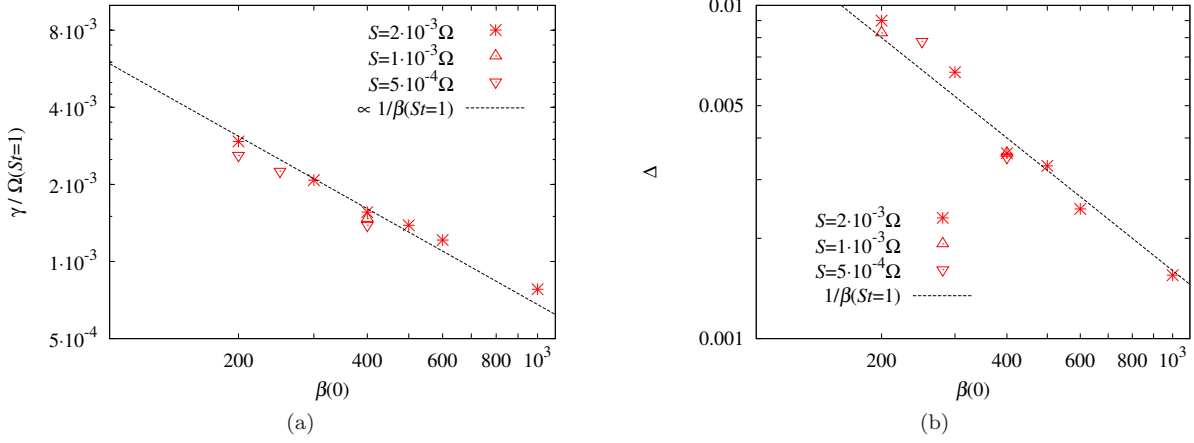


Figure 9. (a) Inverse decay time scale γ/Ω for the mirror turbulence, based on fitting the data to the decay law (37), vs. $\beta(0)$, at various values of initial S (on which it manifestly does not depend). The fit $\gamma = 0.19\Omega/\beta(|S|t=1)$ is shown as a dotted line and is manifestly a good description of the data, supporting equation (36). (b) Mean pressure anisotropy $\Delta = (p_{\parallel} - p_{\perp})/p$ for the same decaying runs. The mirror-marginal level, $\Delta = 1/\beta(|S|t=1)$, is shown as a dotted line, confirming that decaying mirror turbulence stays marginal, as argued in section 2.4.

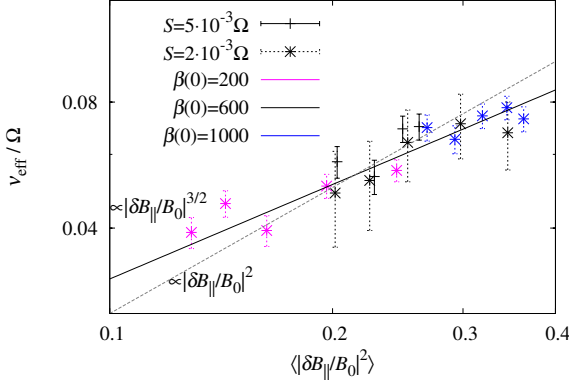


Figure 10. Effective collisionality ν_{eff}/Ω vs. $\langle |\delta B_{\parallel}/B_0|^2 \rangle$ (mean over the box) at various times during the decay stage for the mirror turbulence (section 2.4) and at various values of initial S and β . The solid straight line shows the fit $\nu_{\text{eff}}/\Omega = 0.17\langle |\delta B_{\parallel}/B_0|^2 \rangle^{3/4}$ and the dashed one $\nu_{\text{eff}}/\Omega = 0.25\langle |\delta B_{\parallel}/B_0|^2 \rangle$, corresponding to the scalings (33) and (34), respectively.

γ^{-1} (assuming $\delta B_{\parallel}/B_0 \sim 1$ at $t = t_0$) as firehose fluctuations did in section 2.2, but the decay is slower than exponential.

2.4.2 Numerical results

Figure 8 shows the time history of a numerical experiment analogous to the one described in section 2.2, except starting in a mirror-marginal state populated by mirror fluctuations. A snapshot of the mirror fluctuation field in free decay is shown in figure 7b.

In line with the above arguments, we see mirror fluctuations decay consistently with equation (37), at least for a reasonable initial period (figure 8a)—although at the level of precision and asymptoticity that we can afford in these simulations, we cannot distinguish definitively between the decay law (37) and an exponential decay $\langle \delta B_{\parallel}^2/B_0^2 \rangle \propto e^{-\gamma t}$.

The decay time γ^{-1} scales as predicted in equation (36) (see figure 9a), while the pressure anisotropy stays mirror-marginal (figure 8b; see also figure 9b).¹⁰

The comparison of the effective collisionality with the scalings (33) and (34) is shown in figure 10. The overall scaling should be closer to $\nu_{\text{eff}} \propto |\delta B_{\parallel}/B_0|^2$, because it is the weighted average (35), but, unfortunately, the quality (and/or the degree of asymptoticity) of the data does not allow for a clear differentiation between the two scalings.

This, with some caveats, our numerical results appear to be largely consistent with the simple description of the decaying mirror turbulence proposed above.

3 PRESSURE ANISOTROPY AND MICROTURBULENCE IN A REVERSING SHEAR FLOW

Let us now investigate the more “general” scenario in which the shear S acts for a while—typically for a time of order S^{-1} —and then reverses, with the new, equal and opposite, shear acting for another time of order S^{-1} , again reversing, etc. (in general, the shear will also change magnitude, but we will not study such a situation here). Arranging such a sequence is a small step toward a local model of a macroscopic turbulent flow.

¹⁰ In figure 8, the anisotropy appears to stabilise considerably above the marginal level in Stage 2 (secular growth), but in fact, if we continued the driven stage longer than one shear time, it would slowly decay towards the marginal level (Kunz et al. 2014). Note further that the fast relaxation to 0 that occurs immediately after the shear is switched off occurs on a time scale that is consistent with the effective collision rate at the moment of switch-off: from figure 8a, $S/\nu_{\text{eff}} \sim 0.02$. The subsequent approach to the mirror-marginal level is from the stable side ($\Delta \rightarrow 1/\beta$ from below). The latter behaviour is analogous to what happens in the case of decaying firehose turbulence (see footnote 7).

3.1 From firehose to mirror

Consider first the case in which the shear switches from positive (firehose-unstable) to negative (mirror-unstable). As the mean field starts growing, a system with no initial microscale fluctuations would develop a positive pressure anisotropy and go mirror-unstable, as it did in the sheared initial phase of the numerical experiment shown in figure 8. In contrast, in the numerical experiment we are about to describe here, the shearing of the mean field to larger values happens against the background of pre-existing firehose fluctuations, which will in general evolve in time and thus contribute to the evolution of the pressure anisotropy.

This evolution satisfies equation (8), except the direction of the shear is now reversed:

$$\frac{1}{3} \frac{d\Delta}{dt} + \nu_{\text{eff}} \Delta = \left| \frac{d \ln B_0}{dt} \right| + \frac{1}{2} \frac{d\langle |\delta \mathbf{b}|^2 \rangle}{dt}. \quad (38)$$

Note that at least initially, there are no mirror fluctuations (no δB_{\parallel}) because at the moment of shear reversal the system is at the firehose threshold and so is mirror-stable.

There are two possible scenarios, depending on the magnitude of β .

3.1.1 Theoretical expectations: case of $\beta \ll \Omega/S$

In this case, the firehose fluctuations at $St \sim 1$ are saturated at $\langle |\delta \mathbf{b}|^2 \rangle \sim (\beta S/\Omega)^{1/2}$ (section 2.1.2). As we found in section 2.2, in the absence of an externally imposed shear, they will decay at the rate $\gamma \sim \Omega/\beta$. It is reasonable to expect that their evolution in the presence of a shear that does not drive them will be no different provided this shear is slow compared to their free decay. Namely, the second term in the right-hand side of equation (38) is larger than the first provided

$$\frac{d\langle |\delta \mathbf{b}|^2 \rangle}{dt} \sim \gamma \langle |\delta \mathbf{b}|^2 \rangle \gg \left| \frac{d \ln B_0}{dt} \right| \sim |S|. \quad (39)$$

With $\langle |\delta \mathbf{b}|^2 \rangle \sim (\beta |S|/\Omega)^{1/2}$ initially, this is the case in precisely the regime that we are considering, $\beta \ll \Omega/S$. The firehose fluctuations will then decay freely according to

$$\langle |\delta \mathbf{b}|^2 \rangle \sim \left(\frac{\beta |S|}{\Omega} \right)^{1/2} e^{-\gamma t}, \quad (40)$$

until $\langle |\delta \mathbf{b}|^2 \rangle$ becomes small enough for the condition (39) to stop being satisfied. This happens at the time t_{decay} when

$$\langle |\delta \mathbf{b}|^2 \rangle \sim \frac{|S|}{\gamma} \sim \frac{\beta |S|}{\Omega} \Rightarrow t_{\text{decay}} \sim \frac{\beta}{\Omega} \ln \frac{\Omega}{\beta |S|}, \quad (41)$$

i.e., generally in just a fraction of one shear time. After this, the remaining firehose fluctuations can simply be sheared away (on the time scale $|S|t \sim \langle |\delta \mathbf{b}|^2 \rangle \sim \beta |S|/\Omega \ll 1$), the pressure anisotropy is no longer pushed towards the firehose-marginal level by their free decay, but instead pushed up by the shear towards the mirror threshold, and the system can go mirror unstable as it does in the case of no initial fluctuations, with the mirror-instability evolution proceeding as before (see section 2.3).

3.1.2 Theoretical expectations: case of $\beta \gg \Omega/S$

At such ultra-high betas, the firehose fluctuations at $St \sim 1$ are $\langle |\delta \mathbf{b}|^2 \rangle \sim 1$ and, once the shear is reversed, their free

decay would be too slow to compete with the new shear (i.e., the condition (39) is broken from the outset). The dominant balance in equation (38) is then between the two terms in the right-hand side:

$$\frac{1}{2} \frac{d\langle |\delta \mathbf{b}|^2 \rangle}{dt} \approx - \left| \frac{d \ln B_0}{dt} \right| \sim -|S|. \quad (42)$$

Thus, the firehose fluctuations are sheared away secularly,

$$\langle |\delta \mathbf{b}|^2 \rangle \sim 1 - St, \quad (43)$$

and will be gone after approximately one shear time. This means that during (most of) the time that the reversed shear acts, *the decay of the residual firehose fluctuations can offset the increase of the mean field by shear—and so the system need not cross the mirror threshold and go unstable*. By the time the residual firehose reservoir is exhausted and the system is ready for mirror instability, it will be too late as the shear will, in general, reverse again.

3.1.3 Numerical results

The scenario proposed above is broadly confirmed by the numerical experiments with reversing the shear (the analogue of the one described in section 2.2.2, but the shear equal to $-S$, rather than 0, for $|S|t > 1$). This is documented in figure 11. The two values of beta, $\beta = 200$ and 600, for which the evolution of the fluctuation level is shown in figure 11a correspond approximately (although not asymptotically) to the regimes discussed in sections 3.1.1 and 3.1.2, respectively. We see that the onset of the mirror-unstable regime (manifested by the growth of $\langle \delta B_{\parallel}^2 \rangle$ in figure 11a and of the pressure anisotropy Δ in figure 11b) is delayed in both cases—and for a longer time at higher β . Runs with other values of β confirm this trend (see figure 11b) and in particular the assertion in section 3.1.2 that at high enough β , the onset of the mirror instability is delayed by approximately one shear time.

Note that, in the ultra-high-beta regime, while the mean field decays and then grows again, the mean magnitude of the magnetic field (i.e., the total magnetic energy, including firehose fluctuations) stays essentially constant (see figure 11c): in the driven-firehose regime ($|S|t < 1$, $S > 0$), this is because the stage of the secular firehose growth compensating the decrease of the mean field extends over an entire shear time (see section 2.1), whereas in the decaying-firehose regime ($|S|t > 1$, $S < 0$), the fluctuations' decay by being sheared away is compensated by the growth of the mean field (section 3.1.2).

Snapshots of the firehose field being sheared away are shown in figures 3d and e ($St = 1.4$ and $St = 2$, respectively); while figure 3f shows the (rather feeble) mirror field that comes to replace the firehose turbulence.

3.2 From mirror to firehose

Now consider the opposite situation to section 3.1, *viz.*, a switch from negative (mirror-unstable) shear to positive (firehose-unstable) one. The results of this numerical experiment, illustrated by figure 12, are perhaps not as newsworthy as those of the previous one (section 3.1). In summary, after the shear is reversed, mirror fluctuations decay, the system is driven through the firehose threshold and firehose

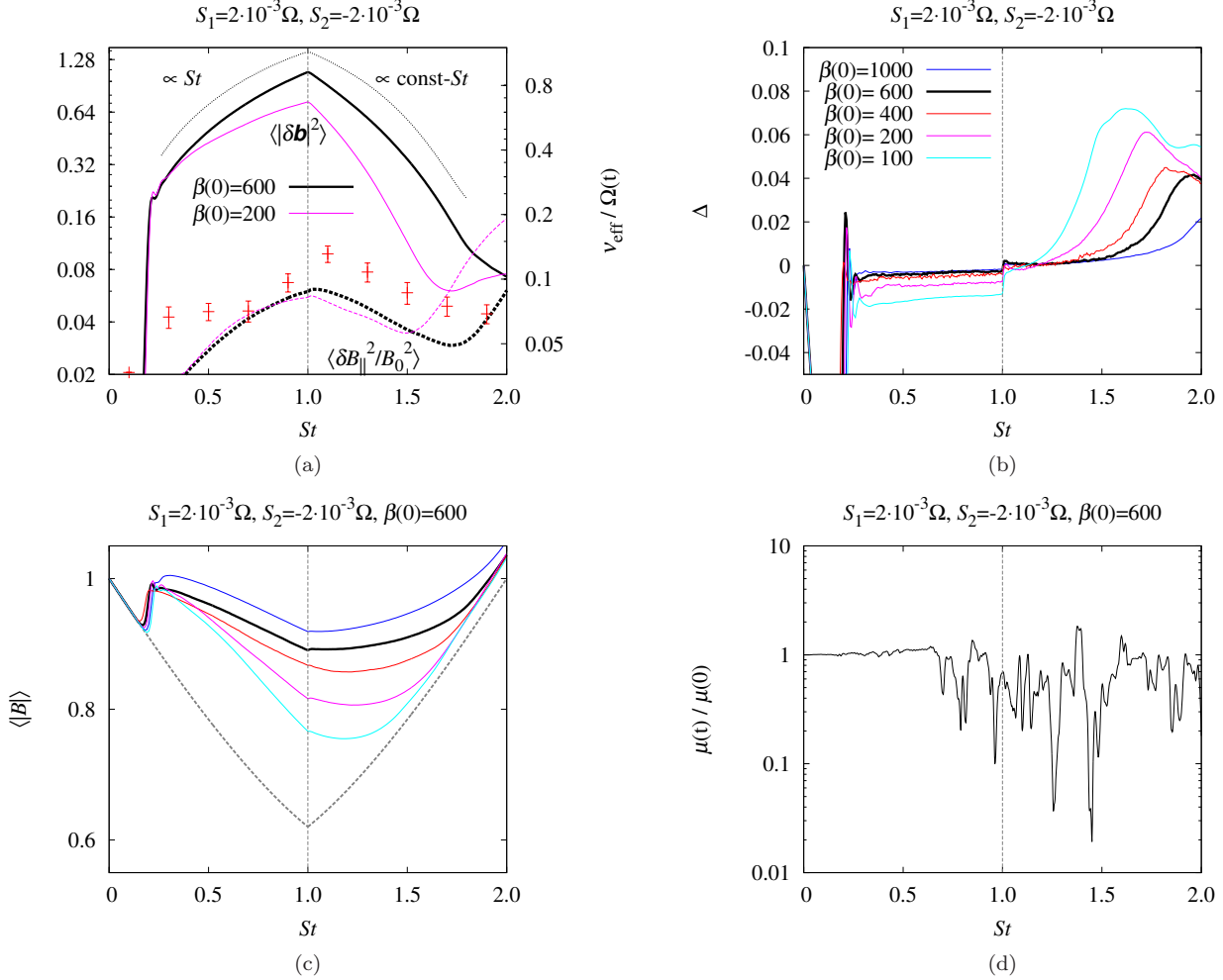


Figure 11. Same as figure 4, but with reversed shear in the second phase (driving firehose, then mirror): from $S = 2 \times 10^{-3}\Omega$ until $St = 1$ to $S = -2 \times 10^{-3}\Omega$ afterwards; $\beta(0) = 600$. Same quantities are shown, with the following differences. (a) Time evolution of both the mirror perturbations, $\langle \delta B_{\parallel}^2 / B_0^2 \rangle$ (dotted lines), and the firehose ones, $\langle |\delta \mathbf{b}|^2 \rangle$ (solid lines), is given for two values $\beta(0) = 600$ (black, bold) and $\beta(0) = 200$ (magenta), showing that the onset of the mirror-unstable regime is delayed at higher β ; the effective collisionality ν_{eff} is shown for the $\beta(0) = 600$ case. (b) Time evolution of the pressure anisotropy $\Delta = (p_{\perp} - p_{\parallel})/p$ is given for several values of $\beta(0)$. At $St < 1$, each of these simulations hovers near its respective firehose threshold, $\Delta = -2/\beta(t)$, similarly to figure 4b (thresholds not shown here to avoid clutter). At $St > 1$, Δ starts growing towards the mirror threshold, but that happens later at higher β . (c) Time evolution of the mean magnitude of the field, $\langle B \rangle = \langle |\mathbf{B}| \rangle$ (as opposed to the magnitude of the mean field, $B_0 = |\langle \mathbf{B} \rangle|$) for the same values of $\beta(0)$ as in (b) (where the legend shows which line corresponds to which $\beta(0)$), showing that at higher β , $\langle B \rangle$ barely changes throughout both the firehose and mirror regimes. The magnitude of the mean field, $|\langle \mathbf{B} \rangle|$ is shown for the case $\beta(0) = 600$.

fluctuations grow to keep it marginal. The mirrors decay by being sheared away, at least at $\beta \gtrsim \Omega/S$ (see figure 12a). At $\beta \ll \Omega/S$, presumably their free decay would be faster (section 2.4) and would override the shearing, but this regime was not achieved in a pure form at the values $\beta \geq 100$ that we have investigated—presumably a clean asymptotic separation between the shear and the free-decay time scales could be achieved in simulations with much smaller S .

The emergence of the firehose turbulence seems to occur without any delay and quite independently of the fact that there is an initial sea of mirrors, essentially in the same way as it did in section 2.1. This might appear to be a somewhat puzzling result in view of our experience with the system's travails (unsuccessful at ultra-high β) in switching from the firehose to the mirror regime in section 3.1 and with the free decay of the mirror turbulence in section 2.4, where we

argued that the decay of the mirrors could increase mean pressure anisotropy in the system—this begs the question of why then it does not impede or at least slow down the system's journey towards the firehose threshold.

Without claiming to possess a complete theory (any more than we did in the preceding sections), we offer the following considerations to make sense of the observed behaviour. An important difference between mirror and firehose perturbations is the scales at which they develop: whereas the latter grow at $k_{\perp} \rho_i \sim k_{\parallel} \rho_i \sim 1$ (Kunz et al. 2014), the former are generally larger and separated from the Larmor scale by the marginality parameter: $(k_{\perp} \rho_i)^2 \sim k_{\parallel} \rho_i \sim \beta \Delta - 1$ (Hellinger 2007). It is indeed because of this relatively long-scale nature of the mirrors that they fail to scatter particles in their driven secular-growth regime. When the shear is reversed and the mirrors start decay-

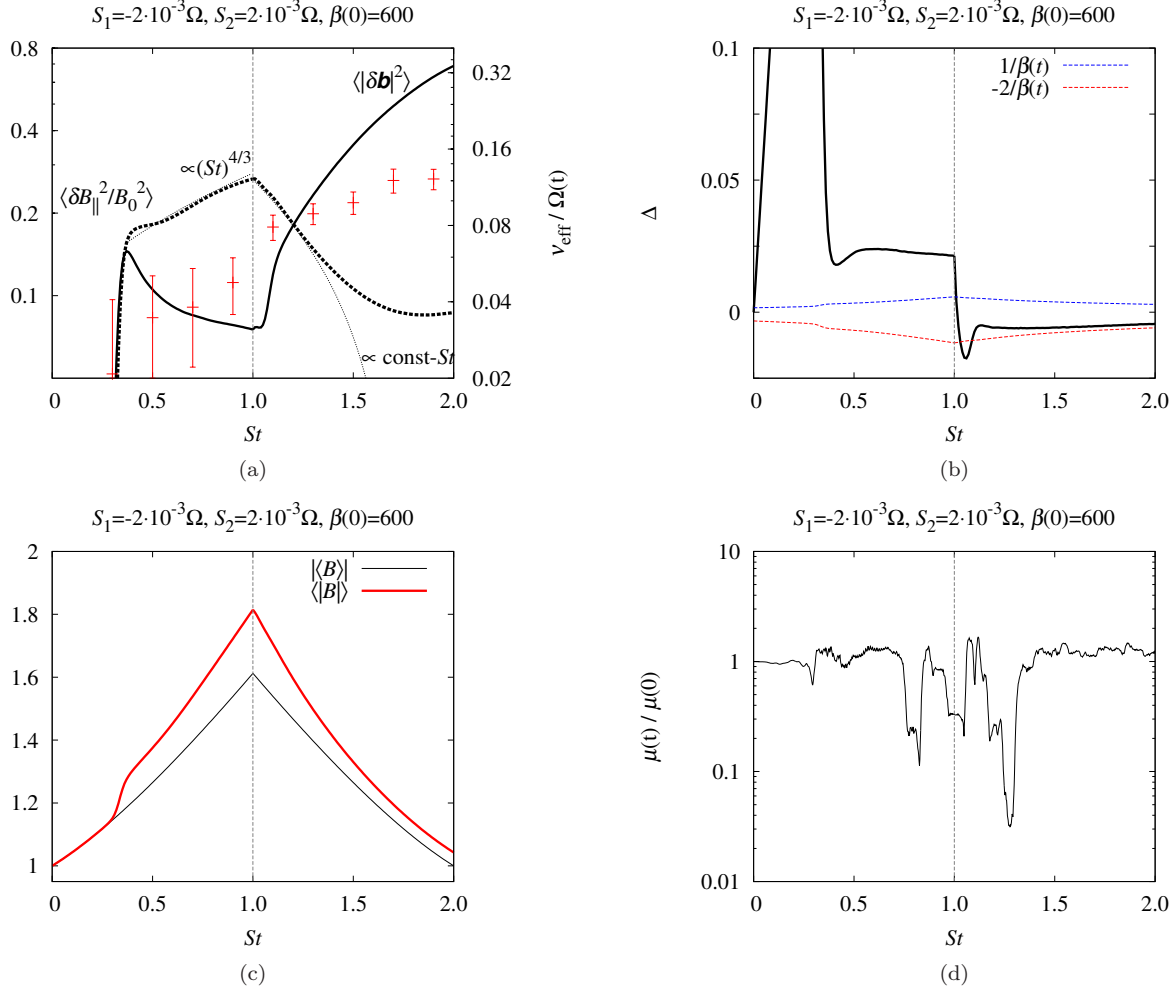


Figure 12. Same as figure 8, but with reversed shear in the second phase (driving first mirror, then firehose): from $S = -2 \times 10^{-3} \Omega$ until $|S|t = 1$ to $S = 2 \times 10^{-3} \Omega$ afterwards; $\beta(0) = 600$. Same quantities are shown with the following differences. (a) Time evolution of both the mirror perturbations ($\langle \delta B_{\parallel}^2 / B_0^2 \rangle$, bold dotted line) and the firehose ones ($\langle |\delta \mathbf{b}|^2 \rangle$, bold solid line) is shown. Dotted lines show the theoretical estimates for the secular growth of driven mirror turbulence at $|S|t < 1$, equation (26), and for its shearing away at $|S|t > 1$, analogously to equation (43). Note the close similarity in the evolution of the system at $|S|t > 1$ with the growing firehose turbulence that started from a pristine state—see the $|S|t < 1$ part of figures 4 and 11. (b) Both the firehose and mirror thresholds are shown (red and blue dotted lines, respectively).

ing, one can think of the relatively long stretches of weaker or stronger field associated with the residual δB_{\parallel} perturbations as “local mean fields” being sheared away, producing local patches of negative pressure anisotropy. These go firehose-unstable, producing Larmor-scale firehose fluctuations on top of the larger-scale, decaying mirror fields. The fact that the latter are somewhat inhomogeneous on the system scale does not bother the firehose fluctuations because of the smallness of their scale. The effect of the released trapped particles sampling larger field and thus increasing the anisotropy, as argued in section 2.4, appears to be overwhelmed in this experiment by the countervailing effect of the external firehose-driving shear (figure 12b).

Snapshots of both the mirror fluctuation field being sheared away and the firehose field emerging in parallel are shown in figures 7c and d, respectively (both at $St = 1.4$).

4 CONCLUSIONS

4.1 Summary

This paper is a contribution to the rapidly expanding body of evidence about the nature and behaviour of pressure-anisotropy-driven ion-scale instabilities (McKean et al. 1993; Quest & Shapiro 1996; Gary et al. 1997, 1998; Hellinger & Matsumoto 2001; Matteini et al. 2006; Kunz et al. 2014; Riquelme et al. 2015; Sironi & Narayan 2015; Hellinger & Trávníček 2015; Hellinger et al. 2015). These studies’ *raison d’être* is to understand the basic ingredients that combine to provide the microphysical (microscale) background to the large-scale dynamics, hence the recent emphasis on driven systems where uniform shear (Kunz et al. 2014; Riquelme et al. 2015) or compression/rarefaction (Matteini et al. 2006; Sironi & Narayan 2015; Hellinger & Trávníček 2015; Hellinger et al. 2015) provide the energy source for the instabilities. The new

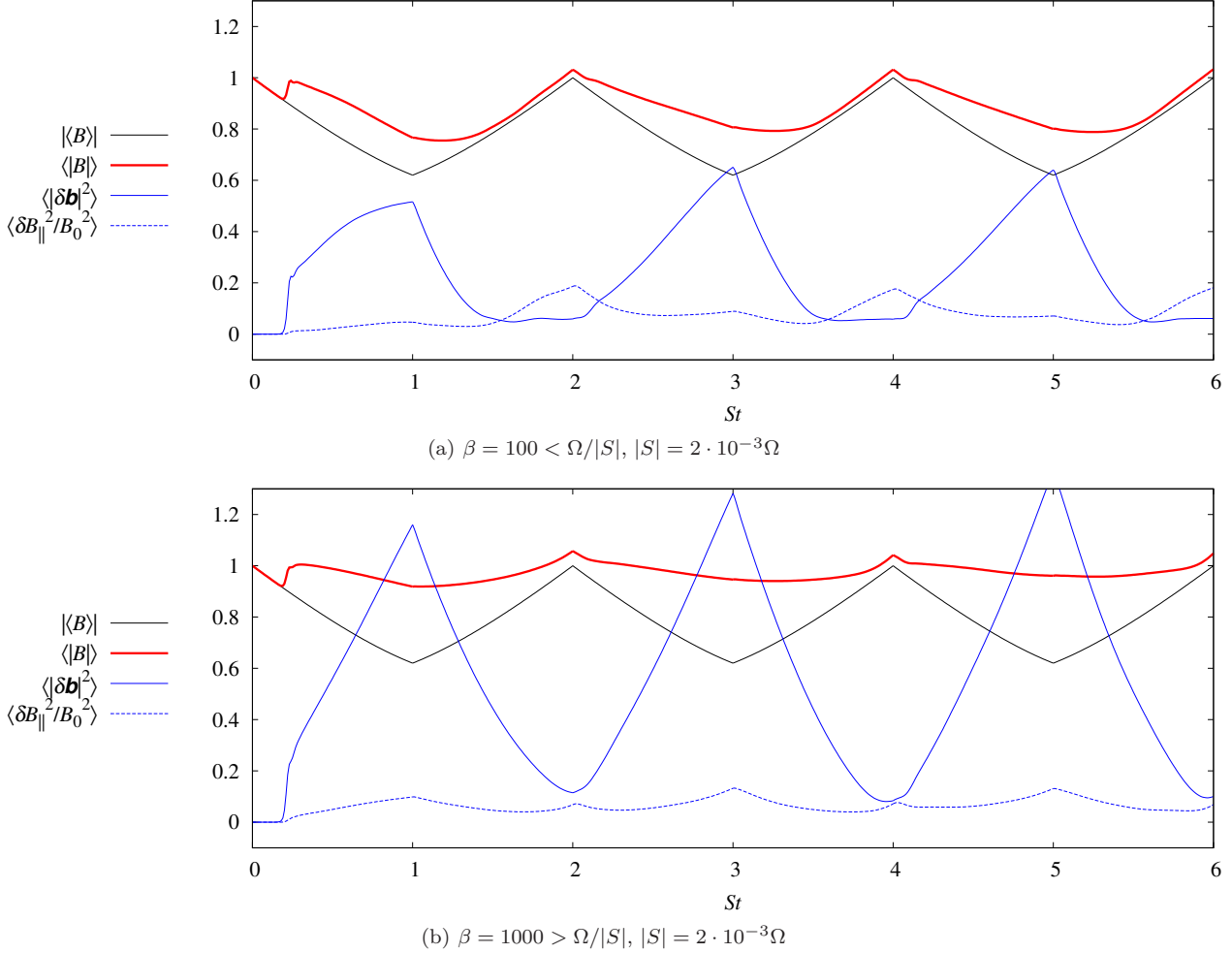


Figure 13. Time evolution of the magnitude of the mean field $\langle |B| \rangle$ (solid black), mean magnitude of the field $\langle B \rangle$ (bold red), firehose fluctuation level $\langle |\delta \mathbf{b}|^2 \rangle$ (solid blue) and mirror fluctuation level $\langle \delta B_{\parallel}^2 / B_0^2 \rangle$ (dashed blue) in two runs where the sign of shear was alternated several times: (a) the case of $\beta < \Omega/|S|$, (b) the case of $\beta > \Omega/|S|$. Note the much-delayed onset (amounting to near-complete suppression) of mirror instability and near constancy of $\langle B \rangle$ in the ultra-high- β case. These plots should be compared to figures 11 and 12(a,c).

step that we have taken here is to investigate what happens when the macroscale flow *changes* and a new macroscale configuration is superimposed on the microscale state left behind by the previous one. We have studied two basic cases: the free decay of microscale fluctuations when the drive—externally imposed shear—is removed and the effect of reversing the shear. We have discovered several interesting and, in our view, quite fundamental phenomena.

- The free decay of both firehose (section 2.2) and mirror (section 2.4) fluctuations is constrained by the same marginal-stability conditions as their growth and saturation in the driven regime. When firehoses decay, magnetic energy decreases and so pressure anisotropy is pushed in the negative direction, towards the firehose threshold. To avoid crossing it, the fluctuations scatter particles and decay exponentially at the rate $\gamma \sim \Omega/\beta$. When mirrors decay, trapped particles are released, sample stronger magnetic fields and the pressure anisotropy is pushed in the positive direction, towards the mirror threshold. Again, the

system avoids crossing this threshold because fluctuations scatter particles (for mirrors, this is unlike what they do in the driven case; see section 2.3) and decay on the same β -dependent time scale as the firehose ones, although the decay law is slower than exponential (equation (37)).

- When the shear is reversed, rather than switched off, the free decay described above competes with fluctuations of one type (mirror or firehose, depending on the sign of the old shear) being sheared away and fluctuations of the other type being driven. A threshold value of β emerges: when $\beta \ll \Omega/S$, the decay rate is large, $\gamma \gg S$, so the free decay is fast compared to macroscale dynamics, old fluctuations quickly disappear and new ones can be made from scratch; in contrast, when $\beta \gtrsim \Omega/S$ (“ultra-high” beta), the old microscale state is only removed on the macroscopic (shear) timescale. The consequences of this are asymmetric for the firehoses (section 3.1) and mirrors (section 3.2): the shearing away of residual firehose turbulence prevents growth of the pressure anisotropy and thus stops the

system from going mirror-unstable; the shearing away of a residual field of mirrors does not stop the system from going firehose-unstable and producing copious firehose fluctuations. We conjectured that the reason for the latter is the relatively large scale of the mirrors, which are “seen” by the Larmor-scale firehoses essentially as local instances of a decreasing mean field.

- By way of illustration of the key features of the moderate- and ultra-high-beta regimes, we refer the reader to figure 13. This shows two numerical experiments, one with $\beta < \Omega/S$, the other with $\beta > \Omega/S$, in which the sign of the shear is alternated several times, so the system goes through multiple successive periods of decaying (firehose-unstable) and growing (mirror-unstable) mean field (this is analogous to successive instances of the experiments described in sections 3.1 and 3.2). The key point is that at ultra-high β , periods of firehose growth and decay alternate, the system spends most of its evolution close to the firehose threshold, the mirror instability is almost completely suppressed, while the mean magnitude of the magnetic field barely changes at all; in contrast, at moderate β , the periods of decaying/growing mean field feature (relatively) lively firehose/mirror fluctuations which however do not survive long past the point when they cease to be driven by the external shear.

- In the context of the emergence of the threshold value of β , we have also carried out a β scan of the driven firehose turbulence, to complement a previous study by Kunz et al. (2014), where only one value of β was used. It has turned out (section 2.1) that the saturation level of firehose fluctuations depends on β , viz., $\langle |\delta \mathbf{b}|^2 \rangle \sim (\beta S / \Omega)^{1/2}$, so when $\beta \gtrsim \Omega/S$, we have $\langle |\delta \mathbf{b}|^2 \rangle \sim 1$. The latter saturation regime takes the system on the order of one shear time to achieve and follows after a long phase of secular growth, during which the pressure anisotropy is pinned at marginal stability purely by the increase in the fluctuation energy, with no appreciable scattering of particles. This is broadly in line with the earlier theoretical argument of Schekochihin et al. (2008) and Rosin et al. (2011), although unlike in their study, the fluctuations are oblique, rather than parallel. We do not as yet have a complete theoretical understanding of this regime, or of the β and S dependence of the saturated firehose amplitude.

4.2 Implications for cosmic magnetogenesis

As large-scale dynamical motions that drive pressure anisotropies are invariably associated with changing the macroscopic magnetic field and since the resulting instabilities give rise to microscopic magnetic fluctuations, the implications of all this for the long-standing problem of the origin (and maintenance) of cosmic magnetism are the obviously relevant and interesting topic to discuss.

4.2.1 Plasma dynamo and ICM viscosity

Let us consider what our results might imply for the operation of “plasma dynamo”—the process of amplification of magnetic fields by turbulence in the ICM or a similar plasma

that is too weakly collisional for an MHD description to be legitimate.

As far as a dynamically weak magnetic field is concerned, macroscale turbulence is a random sequence of rates of strain (stretchings, shears, compressions, etc.—we shall call them all shears for brevity), changing on a macroscopic time scale (“eddy-turnover time”) and leading to a random sequence of increases and decreases in the field strength (magnetic energy). In standard MHD, in 3D, this results on average in an exponential growth of the magnetic energy at the rate comparable to the rms rate of strain of the velocity field (Moffatt & Saffman 1964; Zeldovich et al. 1984; Ott 1998; Chertkov et al. 1999; Schekochihin et al. 2004; Schekochihin & Cowley 2007).

As far as the microphysical world is concerned, a sequence of random shears leads to a sequence of instances of positive or negative pressure anisotropies exciting mirror or firehose fluctuations (which is indeed what is seen in direct numerical simulations of collisionless dynamo; see Rincon et al. 2016). The magnetic energy generated in the form of these fluctuations and/or the anomalous particle scattering caused by them lead to a modification of the magnetic field’s evolution in time. Various scenarios for this were analysed by Mogavero & Schekochihin (2014), focusing especially on two opposing possibilities: growth/decay of the magnetic field caused by the macroscopic plasma motion being slowed down by microscale energy changing to cancel the macroscale evolution vs. anomalous particle scattering causing a decrease in the effective viscosity of the plasma (because dynamic viscosity is $\sim p/\nu_{\text{eff}}$), thereby allowing the turbulent motions to reach smaller scales and hence develop greater rates of strain and amplify the field faster.

We are now in a position to amend this analysis in light of new information provided by Kunz et al. (2014), Riquelme et al. (2015), Rincon et al. (2015) and the present study.

4.2.2 Plasma dynamo at moderate β

As was shown analytically by Rincon et al. (2015) and numerically by Kunz et al. (2014) (see review in section 2.3 of this paper), driven microscale mirrors can keep the plasma at the mirror threshold without scattering particles for as long as a shear time. They do this by sequestering ever more particles in increasingly deep mirror wells so as to prevent the plasma on average from “seeing” that the mean field is increasing. There is no net decrease of magnetic energy to cancel the mean-field growth and so the mirror instability does not change the local rate of growth of the field, so long as the “eddies” that give rise to these growth episodes decorrelate on the same time scale as they “turn over.”¹¹ Thus, it is probably a good assumption that growth episodes during which plasma crosses the mirror threshold are typically

¹¹ Some level of scattering can occur if a growth episode lasts so long that the mirrors reach $\delta B/B \sim 1$ (Kunz et al. 2014; Riquelme et al. 2015). Then the local effective viscosity of the plasma drops and the “eddy” that caused the growth of the field breaks up into smaller “eddies”—these can produce even faster growth, but also decorrelate very quickly. See the discussion that is about to follow of similar behaviour in the firehose regime.

associated with large-scale motions that stay correlated on approximately one shear time, produce local regions filled with mirror wells and do not scatter particles.

In contrast, driven firehose fluctuations in the moderate- β regime ($\beta \ll \Omega/S$) do start scattering particles very quickly after the instability is triggered (see Kunz et al. 2014 and section 2.1 of this paper) and so should correspondingly decrease the local viscosity of the plasma quasi-instantaneously compared to the time scale of the macroscopic motions.

Let us make some estimates in the modelling spirit of Mogavero & Schekochihin (2014). In the driven firehose regime (shear S attempting to decrease mean field), the effective collisionality of the plasma is $\nu_{\text{eff}} \sim S\beta$ (equation (15)). Then the effective dynamical viscosity is

$$\mu_{\text{eff}} \sim \frac{p}{\nu_{\text{eff}}} \sim \frac{B^2/8\pi}{S}. \quad (44)$$

Assuming velocities U at the (macroscopic) outer scale L and a Kolmogorov cascade supporting a constant flux of energy

$$\varepsilon \sim \frac{\rho U^3}{L}, \quad (45)$$

where ρ is the mass density of the plasma, the largest rate of strain will be at the cutoff scale set by the effective viscosity (44): by simple dimensional analysis,

$$S \sim \left(\frac{\varepsilon}{\mu_{\text{eff}}}\right)^{1/2} \sim \text{Ma} \left(\frac{U}{L} \nu_{\text{eff}}\right)^{1/2}, \quad (46)$$

where $\text{Ma} = U/v_{\text{th}}$ is the Mach number (v_{th} is the ions' thermal speed) and we have used $p \sim \rho v_{\text{th}}^2$. Since $\nu_{\text{eff}} \sim S\beta$, we get

$$S \sim \frac{U}{L} \text{Ma}^2 \beta \equiv \frac{U}{L} \text{Re}_{\text{eff}}^{1/2} \Rightarrow \text{Re}_{\text{eff}} = \text{Ma}^4 \beta^2, \quad (47)$$

where Re_{eff} is the effective Reynolds number.¹² Another way to write the above estimate for the dominant shear is

$$S \sim \frac{\varepsilon}{B^2/8\pi}, \quad (48)$$

i.e., weak magnetic fields are subject to faster change and the rate of this change is equal to the rate of power injection into the turbulence:

$$\frac{d}{dt} \frac{B^2}{8\pi} \sim S \frac{B^2}{8\pi} \sim \varepsilon. \quad (49)$$

This was the basis for a prediction by Mogavero & Schekochihin (2014) that, in such an enhanced-collisionality plasma, magnetic energy can grow to equipartition with kinetic energy of the motions ($B^2/8\pi \sim \rho U^2/2$) in just one large-scale turnover time $\sim L/U$. However, we now know (section 2.2) that the collisionality-enhancing firehose fluctuations can only be maintained for a short time ($\sim \gamma^{-1} \sim \beta/\Omega \ll S^{-1}$) if they are not driven, as they indeed are not, in the instances of growing field. Therefore, the regions of high- Re_{eff} turbulence enabled by the firehose fluctuations are likely to break up and

dissipate the macroscale field-decreasing motion that drove the firehoses in the first place more efficiently than they are to amplify the field.

With the above estimates in hand, we can work out what it takes for the condition $\beta \ll \Omega/S$ to be satisfied: noticing that $\Omega = v_{\text{th}}/\rho_i = v_{\text{th}}/d_i\sqrt{\beta}$, where $d_i = c/\omega_{\text{pi}}$ is the ion inertial scale, independent of the magnetic field, we get

$$\beta \ll \frac{\Omega}{S} \Leftrightarrow \beta \ll \left(\frac{L}{d_i} \frac{1}{\text{Ma}^3}\right)^{2/5} \equiv \beta_c. \quad (50)$$

It is not hard to check that the viscous cutoff scale for this turbulence, $l_{\text{visc}} \sim L \text{Re}_{\text{eff}}^{-3/4}$, is safely larger than ρ_i at these values of β .

Thus, assuming $\beta \ll \beta_c$, the moment a large-scale “eddy” somewhere tries to decrease the magnetic field, the plasma there explodes into a sea of firehoses, locally acquires a large effective Reynolds number as per equation (47), and so the offending “eddy” quickly breaks up into smaller “eddies,” some of which might try to decrease the field further and so would break up into even smaller ones, and others to increase it, which would near-instantly cause them to regain viscosity and be damped by it (the firehose fluctuations that were providing the increased collisionality quickly decay away in this regime; see section 2.2).

To summarise, one might imagine the turbulent plasma dynamo in this regime as a sequence of random macroscale shears, some of which increase the macroscale magnetic field largely unimpeded but at the price of infesting it with microscale mirror “bubbles,” while others attempt to decrease it but instantly break up. Overall, this picture appears to favour magnetic-field amplification over its decay and thus should be a more efficient dynamo than its MHD counterpart—good news for fast cosmic magnetogenesis.

We stress again that, because we have assumed $\beta \ll \Omega/S$, the firehose and mirror fluctuations decay quickly when the shear goes away or its direction changes (see sections 2.2 and 2.4) and so local patches of the system where these shears operate switch quasi-instantaneously from a firehose- to a mirror-dominated state, or vice versa.

4.2.3 Plasma dynamo at ultra-high β

At ultra-high β , viz., $\beta \gtrsim \Omega/S$, the main difference is that the system cannot quickly “forget” about its previous microscale state when the macroscale shear changes: namely, it has to rely on the new shear not only to amplify or diminish the macroscale magnetic field but also to shear away the microscale fluctuations left in the wake of the previous shear. By the time the old fluctuations are gone, the new shear decorrelates and changes again.

As we saw in section 3.1, the shearing away of residual firehose fluctuations that occurs in the regions where the macroscale motion tries to amplify the field effectively prevents pressure anisotropy from growing enough to cross the mirror threshold. Therefore, in the ultra-high- β regime, the system can largely avoid being mirror unstable and a given shear can increase magnetic field with impunity (as long as it does not last longer than a shear time and occurs after a firehose-unstable episode; section 3.1). However, as we saw in sections 2.2 and 3.1, the decaying firehose turbulence vigor-

¹² Note that the fact that Re_{eff} “knows” about the local value of β and so the instantaneous strength of the magnetic field can set the size of the dominant rate of strain [equation (48)] means that plasma dynamo is *never* strictly kinematic.

ously scatters particles. According to equation (21), it does so at the rate $\nu_{\text{eff}} \sim \Omega$ after the shear is reversed, at least for a large initial fraction of the shear time during which the residual firehose fluctuation level is still $\langle |\delta \mathbf{b}|^2 \rangle \sim 1$. The plasma in such a collisional regime is nearly unmagnetised. Using equation (46) with $\nu_{\text{eff}} \sim \Omega$, we get

$$S \sim \frac{U}{L} \text{Re}_{\text{eff}}^{1/2}, \quad \text{Re}_{\text{eff}} \sim \text{Ma} \frac{L}{d_i} \frac{1}{\sqrt{\beta}}. \quad (51)$$

Note that it immediately follows that the plasma is in the ultra-high- β regime provided

$$\beta \gtrsim \frac{\Omega}{S} \quad \Leftrightarrow \quad \beta \gtrsim \beta_c, \quad (52)$$

where the threshold value β_c is again given by equation (50).

The large shears generated in such high- Re_{eff} regions will, if they are locally field-decreasing, produce more firehose fluctuations or, if they are field-increasing, shear them away and thus return to low collisionality and high viscosity, which will promptly damp away these shears. Again, somewhat analogously to what we saw happen in the driven-firehose regions analysed in section 4.2.2, the integrity of the macroscale motions is undermined by the firehose turbulence.

Consider now the instances of decaying field against the background of residual mirror fluctuations. In section 3.2, we saw that these mirrors do not matter: firehose fluctuations are wont to grow on scales smaller than the mirrors and so the latter “look” like a local mean field to the former. As the driven firehose fluctuations in the ultra-high- β regime grow secularly for about a shear time, rather than scattering particles (section 2.1), the decrease of the mean field in the firehose regime is accompanied by the compensating increase of the firehose turbulence and the total magnetic energy does not change.

To summarise, in the ultra-high- β regime, plasma motions attempting to decrease the mean field do not diminish the total magnetic energy because it is transferred to firehose fluctuations; the motions attempting to amplify the field, while prevented by those firehose fluctuations from rendering the plasma mirror-unstable, are quickly broken up because the firehose turbulence scatters particles and thus radically diminishes the effective viscosity of the plasma. It is hard to tell without a more quantitative theory how much field amplification these motions can accomplish before they are broken up and damped away. In the absence of such a theory, while it is not clear how quickly the field is amplified, it appears reasonably certain that decreasing the field is quite hard.

4.2.4 β threshold

One key conclusion of this work is that, since the rate of free decay of microscale fluctuations depends inversely on β (sections 2.2 and 2.4), in ultra-high- β plasmas it is quite difficult to get rid of magnetic energy once it has been generated. The threshold value of β for this regime is $\beta_c \sim \Omega/S$, or, using $\Omega = v_{\text{th}}/d_i\sqrt{\beta}$,

$$\beta_c \sim \left(\frac{v_{\text{th}}}{S d_i} \right)^{2/3} \sim \left(\frac{L}{d_i} \frac{1}{\text{Ma}} \right)^{2/3}, \quad (53)$$

where the last expression was obtained via the estimate $S \sim U/L$, with U and L being the velocity and scale of the

macroscopic motions that provide the local shear. For standard core-ICM conditions (see, e.g., Enßlin & Vogt 2006; Schekochihin & Cowley 2006; Kunz et al. 2011; Rosin et al. 2011; Zhuravleva et al. 2014), taking $L \sim 10 \text{ kpc} \sim 10^{17} \text{ km}$, $d_i \sim 10^3 \text{ km}$, $v_{\text{th}} \sim 10^3 \text{ km/s}$, $\text{Ma} \sim 0.1$, we find $\beta_c \sim 10^9$, corresponding to an ICM magnetic field of $B \sim 10^{-9} \text{ G}$.

However, as we have seen in section 4.2.2, the maximum rate of strain S in the plasma flow may itself depend on β because of the modification of the effective viscosity by anomalous particle scattering off microscale fluctuations. As a result, the estimate for the β threshold is modified and given by equation (50) (see also equation (52)). Using the same fiducial ICM parameters, this value is $\beta_c \sim 10^7$, corresponding to $B \sim 10^{-8} \text{ G}$. While this is weaker than the observed fields (which tend to be $B \sim 10^{-6} \text{ G}$; see, e.g., Carilli & Taylor 2002, Govoni & Feretti 2004, Vogt & Enßlin 2005), it is substantially greater than even the most optimistic end of the range in which the primordial seed field is believed to lie ($B \sim 10^{-21} - 10^{-9} \text{ G}$; see Durrer & Neronov 2013).

Thus, whichever estimate one uses, the “ultra-high” beta is in fact not all that high and both beta ranges considered in this paper should therefore be relevant to our understanding of cosmic magnetogenesis, with the dynamo in the ultra-high-beta regime possibly responsible for most of the magnetic-field amplification from the primordial seed.

ACKNOWLEDGMENTS

We are grateful to S. C. Cowley for many important discussions, without which this work would not have been conceived. We also thank P. Catto, F. Parra, E. Quataert, F. Rincon, and A. Spitkovsky for valuable comments. M. W. K. was supported by a Lyman Spitzer, Jr. Fellowship and by the Max-Planck–Princeton Center for Plasma Physics. He thanks Merton College, Oxford, for its support of his visits to Oxford. All three authors also thank the Wolfgang Pauli Institute, Vienna, for its hospitality and support.

REFERENCES

- Bale S. D., Kasper J. C., Howes G. G., Quataert E., Salem C., Sundkvist D., 2009, *Phys. Rev. Lett.*, 103, 211101
- Carilli C. L., Taylor G. B., 2002, *ARA&A*, 40, 319
- Chandran B. D. G., Dennis T. J., Quataert E., Bale S. D., 2011, *ApJ*, 743, 197
- Chertkov M., Falkovich G., Kolokolov I., Vergassola M., 1999, *Phys. Rev. Lett.*, 83, 4065
- Chew G. F., Goldberger M. L., Low F. E., 1956, *Proc. R. Soc. Lond. A*, 236, 112
- Durrer R., Neronov A., 2013, *A&AR*, 21, 62
- Enßlin T. A., Vogt C., 2006, *A&A*, 453, 447
- Forest C. B., et al., 2015, *J. Plasma Phys.*, 81, 345810501
- Fujita Y., 2005, *ApJ*, 631, L17
- Gary S. P., Li H., O’Rourke S., Winske D., 1998, *J. Geophys. Res.*, 103, 14567
- Gary S. P., Wang J., Winske D., Fuselier S. A., 1997, *J. Geophys. Res.*, 102, 27159
- Govoni F., Feretti L., 2004, *Intl. J. Mod. Phys. D*, 13, 1549
- Hellinger P., 2007, *Phys. Plasmas*, 14, 082105

- Hellinger P., Matsumoto H., 2001, *J. Geophys. Res.*, 106, 13215
- Hellinger P., Matteini L., Landi S., Verdini A., Franci L., Trávníček P. M., 2015, *ApJ*, 811, L32
- Hellinger P., Trávníček P., Kasper J. C., Lazarus A. J., 2006, *Geophys. Res. Lett.*, 33, L09101
- Hellinger P., Trávníček P. M., 2015, *J. Plasma Phys.*, 81, 305810103
- Kivelson M. G., Southwood D. J., 1996, *J. Geophys. Res.*, 101, 17365
- Kruskal M., 1958, Project Matterhorn Preprint PM-S-33 (Princeton University)
- Kulsrud R. M., 1983, in Galeev A. A., Sudan R. N., eds, *Handbook of Plasma Physics*, Volume 1, North-Holland, Amsterdam, p. 1
- Kunz M. W., Bogdanović T., Reynolds C. S., Stone J. M., 2012, *ApJ*, 754, 122
- Kunz M. W., Schekochihin A. A., Chen C. H. K., Abel I. G., Cowley S. C., 2015, *J. Plasma Phys.*, 81, 325810501
- Kunz M. W., Schekochihin A. A., Cowley S. C., Binney J. J., Sanders J. S., 2011, *MNRAS*, 410, 2446
- Kunz M. W., Schekochihin A. A., Stone J. M., 2014, *Phys. Rev. Lett.*, 112, 205003
- Kunz M. W., Stone J. M., Bai X.-N., 2014, *J. Comp. Phys.*, 259, 154
- Lyutikov M., 2007, *ApJ*, 668, L1
- Matteini L., Landi S., Hellinger P., Velli M., 2006, *J. Geophys. Res.*, 111, A10101
- McKean M. E., Gary S. P., Winske D., 1993, *J. Geophys. Res.*, 98, 21313
- Meinecke J., et al., 2014, *Nature Phys.*, 10, 520
- Meinecke J., et al., 2015, *PNAS*, 112, 8211
- Meng X., Tóth G., Liemohn M. W., Gombosi T. I., Runov A., 2012, *J. Geophys. Res.*, 117, A08216
- Moffatt H. K., Saffman P. G., 1964, *Phys. Fluids*, 7, 155
- Mogavero F., Schekochihin A. A., 2014, *MNRAS*, 440, 3226
- Ott E., 1998, *Phys. Plasmas*, 5, 1636
- Pantellini F. G. E., 1998, *J. Geophys. Res.*, 103, 4789
- Plihon N., Bousset G., Palermo F., Morales J., Bos W. J. T., Godeferd F., Bourgoin M., Pinton J.-F., Moulin M., Aanesland A., 2015, *J. Plasma Phys.*, 81, 345810102
- Pokhotelov O. A., Sagdeev R. Z., Balikhin M. A., Onishchenko O. G., Fedun V. N., 2008, *J. Geophys. Res.*, 113, A04225
- Quest K. B., Shapiro V. D., 1996, *J. Geophys. Res.*, 101, 24457
- Rebusco P., Churazov E., Böhringer H., Forman W., 2006, *MNRAS*, 372, 1840
- Rincon F., Califano F., Schekochihin A. A., Valentini F., 2016, *arXiv:1512.01461*
- Rincon F., Schekochihin A. A., Cowley S. C., 2015, *MNRAS*, 447, L45
- Riquelme M. A., Quataert E., Verscharen D., 2015, *ApJ*, 800, 27
- Rosin M. S., Schekochihin A. A., Rincon F., Cowley S. C., 2011, *MNRAS*, 413, 7
- Samsonov A. A., Alexandrova O., Lacombe C., Maksimovic M., Gary S. P., 2007, *Ann. Geophys.*, 25, 1157
- Samsonov A. A., Pudovkin M. I., Gary S. P., Hubert D., 2001, *J. Geophys. Res.*, 106, 21689
- Sanders J. S., Fabian A. C., 2013, *MNRAS*, 429, 2727
- Santos-Lima R., de Gouveia Dal Pino E. M., Kowal G., Falceta-Gonçalves D., Lazarian A., Nakwacki M. S., 2014, *ApJ*, 781, 84
- Schekochihin A. A., Cowley S. C., 2006, *Phys. Plasmas*, 13, 056501
- Schekochihin A. A., Cowley S. C., 2007, in Molokov, S., Moreau, R., & Moffatt, H. K. ed., *Magnetohydrodynamics: Historical Evolution and Trends*. Springer, Berlin, p. 85
- Schekochihin A. A., Cowley S. C., Kulsrud R. M., Hammett G. W., Sharma P., 2005, *ApJ*, 629, 139
- Schekochihin A. A., Cowley S. C., Kulsrud R. M., Rosin M. S., Heinemann T., 2008, *Phys. Rev. Lett.*, 100, 081301
- Schekochihin A. A., Cowley S. C., Rincon F., Rosin M. S., 2010, *MNRAS*, 405, 291
- Schekochihin A. A., Cowley S. C., Taylor S. F., Maron J. L., McWilliams J. C., 2004, *ApJ*, 612, 276
- Sharma P., Hammett G. W., Quataert E., Stone J. M., 2006, *ApJ*, 637, 952
- Sharma P., Quataert E., Hammett G. W., Stone J. M., 2007, *ApJ*, 667, 714
- Sironi L., Narayan R., 2015, *ApJ*, 800, 88
- Spence E. J., Reuter K., Forest C. B., 2009, *ApJ*, 700, 470
- Vogt C., Enblin T. A., 2005, *A&A*, 434, 67
- Zeldovich Y. B., Ruzmaikin A. A., Molchanov S. A., Sokolov D. D., 1984, *J. Fluid Mech.*, 144, 1
- Zhuravleva I., Churazov E., Schekochihin A. A., Allen S. W., Arévalo P., Fabian A. C., Forman W. R., Sanders J. S., Simionescu A., Sunyaev R., Vikhlinin A., Werner N., 2014, *Nature*, 515, 85

APPENDIX A: NUMERICAL SET UP

The PEGASUS code used for the numerical experiments reported here is described in detail in Kunz et al. (2014). Here we provide a brief summary and some details relevant to this particular study.

A1 Equations

The code solves, by a standard δf -PIC method, the following equations. The ion distribution function f_i satisfies

$$\left(\frac{\partial}{\partial t} - Sx \frac{\partial}{\partial y} \right) f_i + \mathbf{v} \cdot \nabla f_i + \left[\frac{Ze}{m_i} \left(\mathbf{E} + \frac{\mathbf{v} \times \mathbf{B}}{c} \right) + Sv_x \hat{\mathbf{y}} \right] \cdot \frac{\partial f_i}{\partial \mathbf{v}} = 0, \quad (\text{A1})$$

where S is the externally imposed linear shear, Ze and m_i the ion charge and mass, respectively. The magnetic field \mathbf{B} satisfies Faraday's equation

$$\left(\frac{\partial}{\partial t} - Sx \frac{\partial}{\partial y} \right) \mathbf{B} = -c \nabla \times \mathbf{E} - SB_x \hat{\mathbf{y}}. \quad (\text{A2})$$

The electric field \mathbf{E} satisfies the standard plasma Ohm's law with isothermal electrons:

$$\mathbf{E} = -\frac{\mathbf{u}_e \times \mathbf{B}}{c} - \frac{T_e \nabla n_e}{en_e}, \quad (\text{A3})$$

where T_e is the (constant) electron temperature, the electron flow velocity is computed from the ion flow velocity and the

current (which is found via Ampère's law),

$$\mathbf{u}_e = \mathbf{u}_i - \frac{\mathbf{j}}{en_e} = \frac{1}{n_i} \int d^3\mathbf{v} \mathbf{v} f_i - \frac{c \nabla \times \mathbf{B}}{4\pi en_e}, \quad (\text{A4})$$

and the electron density is related to the ion densities by quasineutrality,

$$n_e = Zn_i = Z \int d^3\mathbf{v} f_i. \quad (\text{A5})$$

These equations are solved in a square box subject to shearing-periodic boundary conditions.

A2 Code units and parameters

The code units are: of time—the inverse initial ($t = 0$) ion cyclotron frequency,

$$[t] = \Omega^{-1}(0) = \frac{m_i c}{ZeB(0)}, \quad [S] = \Omega(0), \quad (\text{A6})$$

of distance—the initial ion inertial length,

$$[x] = [y] = d_i(0) = \frac{c}{\omega_{pi}(0)} = \frac{c}{Ze} \sqrt{\frac{m_i}{4\pi n_i(0)}}, \quad (\text{A7})$$

of velocity (therefore)—the initial Alfvén speed

$$[v] = d_i(0)\Omega(0) = v_A(0) = \frac{B(0)}{\sqrt{4\pi m_i n_i(0)}}, \quad (\text{A8})$$

of magnetic field—the initial magnetic field

$$[B] = B(0), \quad (\text{A9})$$

and of electric field

$$[E] = \frac{v_A(0)B(0)}{c}; \quad (\text{A10})$$

we also normalise particle number densities to their initial values,

$$[n_i] = n_i(0), \quad [n_e] = Zn_i(0). \quad (\text{A11})$$

Under the above normalisations, each run is characterised by three physical dimensionless parameters:

$$\frac{S}{\Omega(0)}, \quad \beta(0) = \frac{8\pi n_i(0)T_i(0)}{B^2(0)}, \quad \tau(0) = \frac{T_i(0)}{ZT_e}, \quad (\text{A12})$$

where $n_i T_i$ is the ion pressure. In all simulations reported here, we chose $\tau(0) = 1$. The initial field was chosen to be

$$\mathbf{B}(0) = \frac{2\hat{x} + 3\hat{y}}{\sqrt{13}}, \quad (\text{A13})$$

so that the mean field was diagonal, $\langle B_x \rangle = \langle B_y \rangle$, at $St = 1/2$.

A3 Shear reversals

The transformation of variables

$$t \rightarrow -t, \quad \mathbf{v} \rightarrow -\mathbf{v}, \quad \mathbf{B} \rightarrow -\mathbf{B} \quad (\text{A14})$$

is exactly equivalent to reversing the sign of shear

$$S \rightarrow -S. \quad (\text{A15})$$

For a number of technical reasons, this proved a convenient ruse to implement the shear reversals for the numerical experiments described in section 3.

A4 Resolution

All runs were done in square boxes whose size was $36 \times 36 \rho_i^2(0)$, where $\rho_i(0) = \sqrt{\beta(0)} d_i(0)$. The cell (mesh) size was $0.125 \rho_i(0)$, with 1024 particles per cell. The time step was $0.01 \Omega^{-1}(0)$.

The exception to this rule were the following runs done at a different resolution and/or in bigger boxes:

- The $\beta = 100$, $S = 2 \times 10^{-3} \Omega$ run with alternating shear, shown in figure 13a: box size $576 \times 576 d_i^2(0) = 57.6 \times 57.6 \rho_i^2(0)$, cell size $1 d_i(0) = 0.1 \rho_i(0)$ (576^2 cells), 576 particles per cell.

- The $\beta = 1000$, $S = 2 \times 10^{-3} \Omega$ run with alternating shear, shown in figure 13b: box size $1152 \times 1152 d_i^2(0) \approx 36.43 \times 36.43 \rho_i^2(0)$, cell size $3 d_i(0) \approx 0.095 \rho_i(0)$ (384^2 cells), 576 particles per cell.

- The $\beta = 600$, $S = 2 \times 10^{-3} \Omega$ runs switching from the mirror to decaying regime and from the mirror to firehose regime, shown in figures 8, 12 and 7: box size $2000 \times 2000 d_i^2(0) \approx 81.65 \times 81.65 \rho_i^2(0)$, cell size $2.6 d_i(0) \approx 0.11 \rho_i(0)$ (768^2 cells), 576 particles per cell.

These did not show any significant differences with the lower-resolution/smaller-box simulations (including those with the same physical parameters), confirming that the latter were adequate.

A5 Effective collision rate

The effective collisionalities ν_{eff} due to particle scattering in firehose and mirror fluctuations are calculated in the following way. We track a number of particles over time intervals $[t, t + \Delta t]$, where $\Delta t = 100/\Omega(t = 0)$, always satisfying $\Delta t > \nu_{\text{eff}}^{-1}$ (confirmed *a posteriori*). For each particle, we calculate the time τ over which its first adiabatic invariant $\mu = v_\perp^2/B$ changes by a factor of 2 (the time evolution of μ is smoothed over time intervals $10/\Omega(0)$, which is of order one Larmor period $2\pi/\Omega(t)$). We assemble a histogram of these times and fit it to an exponential $e^{-\tau/\tau_c}$. We then declare $\nu_{\text{eff}} = \tau_c^{-1}$.